



**HAL**  
open science

# Modelling of earthquake induced pounding between adjacent structures with a non-smooth contact dynamics method

Thomas Langlade, David Bertrand, Stéphane Grange, Gabriel Candia, Juan Carlos de La Llera

## ► To cite this version:

Thomas Langlade, David Bertrand, Stéphane Grange, Gabriel Candia, Juan Carlos de La Llera. Modelling of earthquake induced pounding between adjacent structures with a non-smooth contact dynamics method. Engineering Structures, 2021. hal-03222342

**HAL Id: hal-03222342**

**<https://hal.science/hal-03222342>**

Submitted on 24 May 2023

**HAL** is a multi-disciplinary open access archive for the deposit and dissemination of scientific research documents, whether they are published or not. The documents may come from teaching and research institutions in France or abroad, or from public or private research centers.

L'archive ouverte pluridisciplinaire **HAL**, est destinée au dépôt et à la diffusion de documents scientifiques de niveau recherche, publiés ou non, émanant des établissements d'enseignement et de recherche français ou étrangers, des laboratoires publics ou privés.



Distributed under a Creative Commons Attribution - NonCommercial 4.0 International License



# Modelling of earthquake-induced pounding between adjacent structures with a non-smooth contact dynamics method

T. Langlade<sup>1\*</sup>, D. Bertrand<sup>1</sup>, S. Grange<sup>1</sup>, G. Candia<sup>2</sup>, J. C. de la Llera<sup>2</sup>

<sup>1</sup> *Laboratory GEOMAS EA7495, INSA Lyon, Villeurbanne, France. Corresp\* : [thomas.langlade@insa-lyon.fr](mailto:thomas.langlade@insa-lyon.fr)*

<sup>2</sup> *Research Center for Integrated Disaster Risk Management (CIGIDEN), ANID/FONDAP/15110017, Facultad de Ingeniería, Universidad Del Desarrollo, Santiago de Chile, Chile*

## Abstract

This article presents the kinematic analysis of two adjacent structures with pounding using the framework of finite element dynamic analysis and a non-smooth contact dynamics (NSCD) method for treating contact-impact. The latter consists of a Moreau-Jean implicit integration scheme that uses Moreau's sweeping process and Newton's impact law. Test cases are carried out to prove the efficiency of the implementation and accuracy of the results relative to the widely used penalty method (PM). Furthermore, finite element simulations are compared with shaking table results of two structures susceptible to pounding. Models are steel frames 2.5m to 5m high, 3m in span, have reinforced-concrete slabs, and distant 0 to 5cm. Floor displacements, number and time of occurrence of impacts, as well as shape of the response spectra are in good agreement with experimental observations. Moreover, using the building pounding frame and the NSCD method, an estimation of a constant value for the coefficient of restitution was carried out. It is concluded that the NSCD method is a very numerically efficient tool in terms of reduction of CPU time and description of the impact physics. Consequently, this approach is amenable for fragility analysis of the dynamic response of structures involving a contact-impact phenomenon.

**Keywords:** Earthquake, Building-Pounding, NSCD Method, Experimental Campaign, Contact Algorithm, Sensitivity Analysis

## 1. Introduction

Structural pounding during earthquakes is a recurrent phenomenon in dense urban settings; it occurs when the building separation is insufficient to accommodate the seismically induced displacements. For large earthquakes, the consequences of building pounding can be catastrophic (Figure 1), as it was the case for the Mexico City earthquake of 1985, in which building pounding was the main cause of collapse in at least 15% of collapse observations (Bertero[1]; Rosenblueth and Meli[2]). A survey of the buildings damaged during the 1989 Loma Prieta earthquake (Kasai and Maison[3]) found that pounding occurred primarily in old multi-story masonry buildings, in most cases without separation; in contrast, pounding events were relatively minor in modern constructions. Similarly, structural pounding during the 2017 Puebla earthquake affected mostly very flexible flat-slab systems (Reinoso *et al.*[4]) built prior to 1985, which did not have the minimum separation required by the local seismic code.

Based on observations of the 1985 Mexico City earthquake and the 1989 Loma Prieta earthquake, Jeng *et al.*[7] identified the pounding categories summarized in Figure 2. In each case, the pounding damage can range anywhere from minor architectural damage to partial or total collapse of the building. In addition to an insufficient separation, building pounding occurs due to a combination of other factors (Bertero[8]), most commonly: (i) vague design guidelines and lack of engineering judgement; (ii) ground motion intensities higher than design values; (iii) inadequate structural configurations, particularly buildings with lateral-torsional coupling, soft stories, or low lateral stiffness and



(a) Intermediate floor collapse (mid-story) of Hotel de Carlo in Mexico City, probably caused by pounding against the shorter building to the left; photograph taken after the Mw 8.1 Mexico earthquake[5]



(b) Pounding damage to the reinforced concrete frame and masonry infill building observed during the Mw 7.4, Izmit earthquake, Turkey, 1999[6]

Figure 1: Exemples of building pounding damage during earthquakes

strength; and (iv) pre-existing tilt and ground deformations.

Separation guidelines in current seismic codes aim to avoid contact under maximum inelastic response of each adjacent structure. For instance, ASCE 7-16[9] requires that the maximum inelastic deformation of each building, referred to as  $\delta_{M1}$  and  $\delta_{M2}$ , “shall be determined at critical locations with consideration for translational and torsional displacements of the structures including torsional amplifications, where applicable”, and that the net separation between the structures should be greater than  $\delta_{M1} = \sqrt{(\delta_{M1})^2 + (\delta_{M2})^2}$ . Despite their simplicity and apparent conservatism (e.g., both structures reach simultaneously their maximum deformation in opposite directions), these rules do not guarantee a collision free response, mainly because of the large ground motion and building response uncertainties. Therefore, structural pounding in dense urban areas will probably continue occurring in future earthquakes.

Modelling the seismic response of adjacent buildings subject to pounding remains a very challenging problem, mainly because of the large number of parameters involved and the coarse assumptions typically made to account for the energy transfer between buildings. However, the use of simplified models allows reproducing the key response parameters of the system under different loading conditions. Two modelling approaches for pounding exist in the literature, commonly referred to as the Penalty Method (PM) (Anagnostopoulos[10, 11, 12], Jankowski[13, 14, 15, 16], Naderpour *et al.*[17], Xu *et al.*[18]) and the Lagrange Multipliers Method (LMM) (Papadrakakis and Mouzakis[19, 20], Cole[21], Ambiel *et al.*[22]).

In the former PM approach, the contact forces are modelled through a physical compression gap element between each pair of contact points. Because of its simplicity, the PM approach is widely used in structural engineering and is readily available in most finite element software in the form of one-dimensional nonlinear gap elements. These gap elements allow transferring energy between the two structures and account for local energy dissipation; their main drawback, however, is that the computation of contact forces relies on semi empirical (often non-physical) coefficients, which require experimental validation (Candia *et al.*[23]). For instance, one of the simplest gap element formulations is the Linear Visco-Elastic (LVE) model, where the contact force between two nodes during a collision is given by Equation 1.

$$F(t) = k_s \delta(t) + \xi_d \dot{\delta}(t) \quad (1)$$

Where  $\delta(t)$  is the interpenetration depth (i.e., the amount of overlap between the colliding nodes);  $\dot{\delta}(t)$  the interpenetration rate; and  $k_s$  and  $\xi_d$  are the empirical coefficients representative of the stiffness and damping of the contact

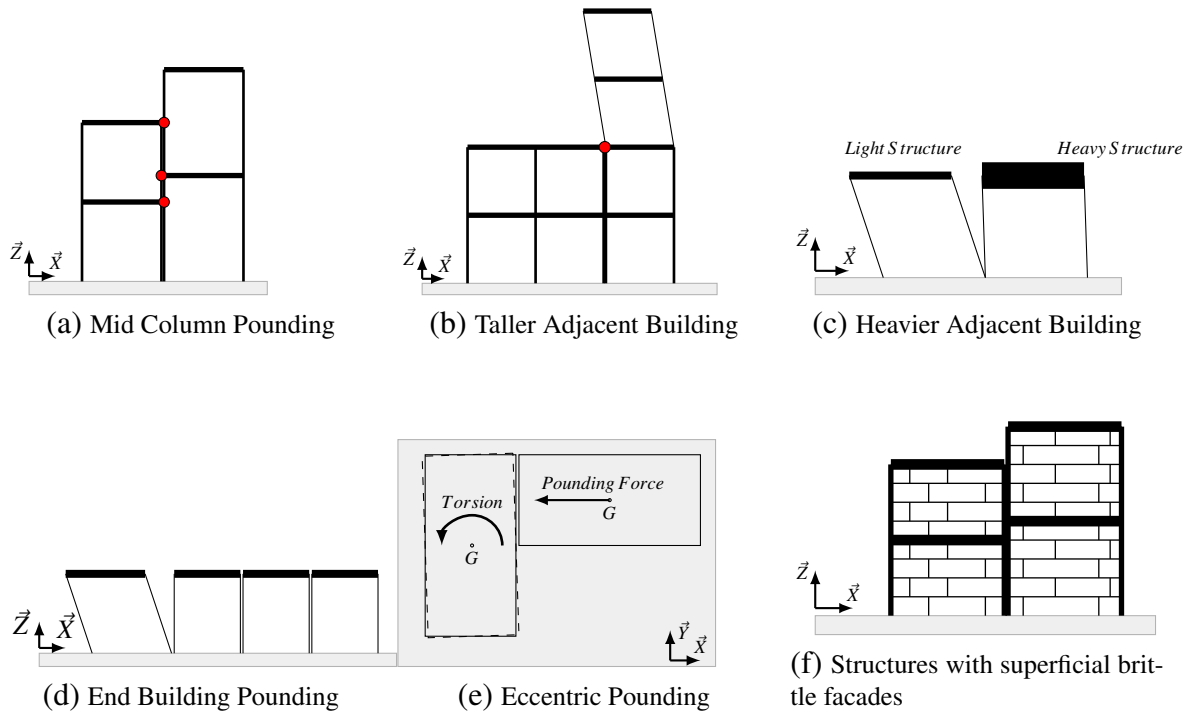


Figure 2: Scheme of critical configurations of structures defined by Jeng *et al.*[7]

interface, respectively. Similar gap element formulations are summarized in Table 1.

Several authors (Jankowski[14, 16], Khatami[24], Anagnostopoulos[10, 12], Xu[18], Crozet[25]) have studied the influence of the gap element parameters and the dynamic response of colliding bodies. For instance, Crozet *et al.*[26] found that the contact stiffness should be greater than ten times the stiffness of the most rigid impacting body, and that the maximum time step for a dynamic analysis should be limited to one-fourth of the smallest vibration periods of the two buildings. These simple rules allow minimizing the contact duration, preserve the system kinematics, and yield acceptable computational runtimes. Studying the response of single degree of freedom (SDOF) systems, Anagnostopoulos[12] found that the contact stiffness has a large effect on the SDOFs accelerations and forces, but a marginal effect on their displacements. Later, based on experimental evidence, Khatiwada *et al.*[27] concludes that the contact stiffness derived from small scale specimens cannot be applied to prototype scale buildings. This latter author is adamant on the limitations of the PM in the building pounding field, highlighting the high sensitivity of the kinematics given the variations in the contact stiffness parameter.

In the Lagrange Multipliers Method (LMM), which derives from the principle of conservation of linear momentum, the contact kinematics is enforced through external loads, and the energy dissipated during inelastic collisions is accounted for by using either the kinematics and internal equilibrium of the system [22, 19, 28], or the coefficient of restitution  $e$  (Acary[29]). These external loads enforce a “strict no-penetration condition”, but they introduce an instantaneous change in the particle velocities, excite high frequency modes, and create large spurious internal forces.

Reported applications of the PM to building pounding problems are significantly larger than LMM applications, in part, because the implementation of LMM solutions is cumbersome, also with respect to convergence and stability. However, the use of LMM is appealing if the coefficient of restitution  $e$  is used since it has a simpler physical interpretation. Therefore, the goal of this article is to present a complementarity method based solution for structural pounding during earthquakes (it has a similar formulation than the LMM); this solution overcomes some of the difficulties found in current LMM implementations, and is based on a single empirical parameter, which simplifies the model definitions.

Indeed, the structural pounding model is based on the Non-Smooth Contact Dynamics (NSCD) algorithm developed by Moreau[30] and extended by Jean[31] and Acary[29, 32, 28, 33] to account for deformable systems. To our knowledge, the use of the NSCD approach to structural pounding problems has not been reported in the literature. In the following sections, the formulation of the NSCD algorithm is presented along with two validation examples: (i) the “bouncing ball test”; and (ii) a plane frame pounding tests, where the NSCD approach is used to reproduce the shaking table response of one and two-story buildings.

Table 1: Main gap element formulations for dynamic pounding analysis

Name	Impact Force $F(t)$	$\xi_d$	$\xi_r$
Hertz Non-Linear (HNL)[34, 35]	$k_s \delta^{\frac{3}{2}}(t)$	/	/
HertzDamp Non-Linear (HDNL)[36]	$k_s \delta^{\frac{3}{2}}(t) + \xi_d \dot{\delta}(t)$	$k_s \left( \frac{8(1-e)}{5e(v_1^- - v_2^-)} \right)$	/
Linear Visco-Elastic (LVE)[12]	$k_s \delta(t) + \xi_d \dot{\delta}(t)$		$-\frac{\ln(e)}{\sqrt{\pi^2 + (\ln(e))^2}}$
Modified Linear Visco-Elastic (MLVE)[16]	Approach period : $k_s \delta(t) + \xi_d \dot{\delta}(t)$ Restitution period : $k_s \delta(t)$	$2\xi_r \sqrt{k_s \frac{m_1 m_2}{m_1 + m_2}}$	$\frac{1-e^2}{e(e(\pi-2)+2)}$
Non-Linear Visco-Elastic (NLVE)[13, 14, 37, 17]	Approach period : $k_s \delta^{\frac{3}{2}}(t) + \xi_d \dot{\delta}(t)$ Restitution period : $k_s \delta^{\frac{3}{2}}(t)$	$2\xi_r \sqrt{k_s \sqrt{\delta} \frac{m_1 m_2}{m_1 + m_2}}$	$\frac{9\sqrt{5}}{2} \frac{1-e^2}{e(e(9\pi-16)+16)}$

$m_1$  and  $m_2$  are nodal masses ;  $e$  is the coefficient of restitution;  $\xi_d$  and  $\xi_r$  are respectively the damping coefficient and damping ratio. Approach period means means that  $\dot{\delta} > 0$ , when relative velocity is positive, thus interpenetration is ongoing. Restitution period means that  $\dot{\delta} \leq 0$ , when relative velocity is negative, thus when bodies are departing from each other.

## 2. NSCD method

This section presents the NSCD approach and integration scheme for the case of two collision-prone linear multi degree of freedom (MDOF) systems. Without significant loss of generality, consider two planar moment resisting frames with lumped masses and net separation  $g_0$ , as shown schematically in Figure 3. Each structure is characterized by a constant mass matrix  $\mathbf{M}_i$ , and a vector of nonlinear internal forces  $\mathbf{P}_i(\mathbf{q}_i, \dot{\mathbf{q}}_i)$  defined in generalized coordinates  $\mathbf{q}_i$ , with  $i = 1, 2$ . Pounding forces may develop at  $n$  discrete locations along the contact interface (i.e., node-to-node contact) between pairs of point-masses on each building, henceforth a contact pair. The impact and energy dissipation on each contact pair are modelled using Newton's impact law and the conservation of linear momentum.

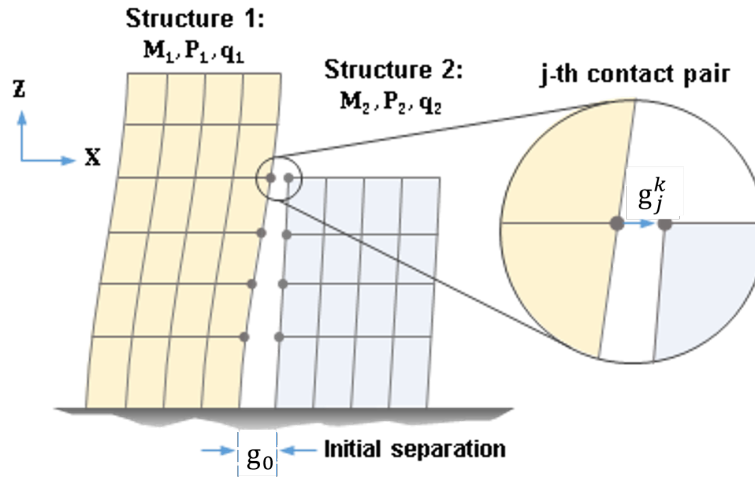


Figure 3: Idealized structures in a deformed position; solid circles represent the contact pairs along the contact interface.

The equations of motion for both systems can be written in augmented form as

$$\mathbf{M}\ddot{\mathbf{q}} + \mathbf{P}(\mathbf{q}, \dot{\mathbf{q}}) - \mathbf{F} = \mathbf{0} \quad (2)$$

where  $\mathbf{q} = [\mathbf{q}_1^T \mathbf{q}_2^T]^T$ ,  $\dot{\mathbf{q}}$  and  $\ddot{\mathbf{q}}$  are the first and second time derivatives of  $\mathbf{q}$ , respectively. The term  $\mathbf{P}(\mathbf{q}, \dot{\mathbf{q}}) = [\mathbf{P}_1^T \mathbf{P}_2^T]^T$  is the vector of internal forces, and the composite mass matrix  $\mathbf{M}$  is the block-diagonal concatenation of matrices  $\mathbf{M}_1$  and  $\mathbf{M}_2$ . The term  $\mathbf{F}$  are a set external forces conjugated in work with  $\mathbf{q}$ , which accounts for static and dynamic loads.

The NSCD integration scheme[31], presented herein, is used to solve Equation 2 in discrete time. The method uses the Moreau-Jean[30] stepping algorithm to step from time  $t_i$  to  $t_{i+1} = t_i + \Delta t$  in addition to the Signorini-Moreau conditions for contact detection. The contribution of Acary[33] allowed for the application of the method to deformable bodies, and highlighted its energy conservation properties[32].

### 2.1. Moreau-Jean stepping algorithm

After integrating Eq. 2 from  $t_i$  to  $t_{i+1}$  and approximating the integral of the nonlinear forces with the midpoint rule, the equation of motion can be written in incremental form as presented in Eq. (4), where  $\mathbf{R}_{k+1}$  stands for the residuals at time  $t_{i+1}$ ,  $\mathbf{G}_i = \int_{t_i}^{t_{i+1}} \mathbf{F} dt$ , and the sub-index  $i + \theta$  denotes the time  $t_{i+\theta} = t_i + \theta\Delta t$ .

$$\int_{t_i}^{t_{i+1}} \mathbf{M}\ddot{\mathbf{q}} dt + \int_{t_i}^{t_{i+1}} \mathbf{P} dt - \int_{t_i}^{t_{i+1}} \mathbf{F} dt = \mathbf{0} \quad (3)$$

$$\mathbf{R}_{k+1} = \mathbf{M}(\dot{\mathbf{q}}_{i+1} - \dot{\mathbf{q}}_i) + \mathbf{P}_{i+\theta}\Delta t - \mathbf{G}_i = \mathbf{0} \quad (4)$$

Expressions for  $\mathbf{q}_{i+1}$ ,  $\dot{\mathbf{q}}_{i+\theta}$ , and  $\mathbf{q}_{i+\theta}$  are shown in Eqs. 5 to 7 based on the Euler- $\theta$  approximation method.

$$\mathbf{q}_{i+1} = \mathbf{q}_i + \dot{\mathbf{q}}_{i+\theta}\Delta t \quad (5)$$

$$\mathbf{q}_{i+\theta} = (1 - \theta)\mathbf{q}_i + \theta\mathbf{q}_{i+1} \quad (6)$$

$$\dot{\mathbf{q}}_{i+\theta} = (1 - \theta)\dot{\mathbf{q}}_i + \theta\dot{\mathbf{q}}_{i+1} \quad (7)$$

The Moreau-Jean algorithm embedded in the NSCD approach uses  $\theta = \frac{1}{2}$ , which results in an implicit integration scheme unconditionally stable relative to regards  $\Delta t$ , similar to the algorithms by Euler and Newmark. If no collisions occur between  $t_i$  and  $t_{i+1}$ , the velocities  $\dot{\mathbf{q}}_{i+1}$  can be obtained solving Eq. (4) (i.e.,  $\|\mathbf{R}_{k+1}\| \leq \epsilon$ , where  $\epsilon$  is a scalar arbitrarily taken close to 0) using the Newton Raphson (NR) algorithm, in which case the velocities in the  $(k + 1)th$  NR iteration can be written as

$$\dot{\mathbf{q}}_{i+1}^{k+1} = \dot{\mathbf{q}}_{i+1}^k - (\mathbf{J}^k)^{-1}\mathbf{R}_{i+1}^k \quad (8)$$

where the Jacobian  $\mathbf{J}^k = \frac{\partial \mathbf{R}_{i+1}^k}{\partial \dot{\mathbf{q}}_{i+1}^k}$  is defined in terms of the tangent damping and stiffness operators  $\mathbf{C}_{i+\theta}^{t,k}$  and  $\mathbf{K}_{i+\theta}^{t,k}$ , respectively, as

$$\mathbf{J}^k = \mathbf{M} + \mathbf{C}_{i+\theta}^{t,k}\Delta t\theta + \mathbf{K}_{i+\theta}^{t,k}\Delta t^2\theta^2 \quad (9)$$

## 2.2. Contact detection and impact forces

If the relative displacements between the buildings are sufficient to close the gap, a collision takes place and a set of impact forces must be added to enforce the no-penetration condition. The separation  $\mathbf{g}_i$  and separation rate  $\dot{\mathbf{g}}_i$  at the  $n$  contact pairs is obtained from the linear relation

$$\mathbf{g}_i = \mathbf{H}\mathbf{q}_i + \mathbf{g}_0 \quad (10)$$

$$\dot{\mathbf{g}}_i = \mathbf{H}\dot{\mathbf{q}}_i \quad (11)$$

where  $\mathbf{H}$  is a kinematic transformation matrix, and  $\mathbf{g}_0 = [g_0^1 g_0^2 \dots g_0^n]^T$  is the initial separation along the contact interface, as shown in Fig 3. When stepping from  $t_i$  to  $t_{i+1}$ , pounding will occur if the predicted gap at time  $t_{i+1}$  is less than zero for any of the contact nodes. In the current NSCD approach, the Signorini-Moreau contact condition is used to predict the separation at time  $t_{i+1}$  as a function of the separation rate shown in Eq. (12), where the constant  $\gamma$  takes a value of  $\frac{3}{2}$ .

$$\hat{\mathbf{g}}_{i+1} = \mathbf{g}_i + \gamma\Delta\dot{\mathbf{g}}_i \quad (12)$$

Based on Newton's impact law, if pounding is detected in a contact pair subset  $\Omega$ , (i.e.,  $\min(\hat{\mathbf{g}}_{i+1,\alpha}) \leq 0$ , with  $\alpha \in \Omega$ ), the rate of separation of each pair is  $\dot{\mathbf{g}}_{i+1} = -e\dot{\mathbf{g}}_i$ , where  $e$  is the coefficient of restitution. To compute the new velocities and enforce the contact kinematics, an impulse vector  $\mathbf{p}_{i+1}$  is added to the equilibrium Equation (4) in addition to the linear constraints in Equations (14) and (15).

$$\hat{\mathbf{R}}_{k+1} = \mathbf{M}(\dot{\mathbf{q}}_{i+1} - \dot{\mathbf{q}}_i) + \mathbf{P}_{i+\theta}\Delta t - \mathbf{G}_i - \mathbf{H}^T\mathbf{p}_{i+1} = \mathbf{0} \quad (13)$$

$$\dot{\mathbf{g}}_{i+1} \leq -e \dot{\mathbf{g}}_i \quad (14)$$

$$\mathbf{p}_{i+1} \geq \mathbf{0} \quad (15)$$

Solving the system's unknowns  $\dot{\mathbf{q}}_{i+1}$  and  $\mathbf{p}_{i+1}$  from Equations (13) to 15 is equivalent to solving a linear optimization problem, for which a vast body of literature exists. Herein, we propose the Gauss-Seidel type solution introduced by Acary[33], which uses a successive elimination of equations. Thus, the impulse at the  $\alpha$ -th contact pair within the  $k$ -th NR iteration is computed as

$$\mathbf{p}_{i+1,\alpha}^k = \frac{1}{\mathbf{W}_{\alpha,\alpha}^k} \left( -\mathbf{b}_{\alpha}^k + \dot{\mathbf{g}}_{\alpha} - \sum_{\beta \neq \alpha} \mathbf{W}_{\alpha\beta}^k \mathbf{p}_{i+1}^k + \mathbf{W}_{\alpha\alpha}^k \mathbf{p}_{i+1,\alpha}^k \right) \geq \mathbf{0} \quad (16)$$

$$\dot{\mathbf{g}}_{\alpha} = -e \mathbf{H} \dot{\mathbf{q}}_{i,\alpha} \quad (17)$$

The terms  $b_{\alpha}^k$  and  $W_{\alpha\beta}^k$ , respectively, the  $\alpha$ -entry and  $(\alpha,\beta)$  entries of matrices  $\mathbf{b}^k$  and  $\mathbf{W}^k$  defined as

$$\mathbf{b}^k = \mathbf{H}(\mathbf{J}^k)^{-1} \mathbf{R}^k + \mathbf{H} \dot{\mathbf{q}}_{i+1}^k \quad (18)$$

$$\mathbf{W}^k = \mathbf{H}(\mathbf{J}^k)^{-1} \mathbf{H}^T \quad (19)$$

A residue on the impact force to ensure the validation of the impulse is introduced with the following formulation proposed by Acary in collaboration with the authors, with  $\rho$  a scalar superior or equal to 1.

$$\mathbf{R}_{\mathbf{c}}^k = \mathbf{p}_{i+1,\Omega_{\alpha}}^k - \max(0, \mathbf{p}_{i+1,\Omega_{\alpha}}^k - \rho(\mathbf{W}_{(\Omega_{\alpha},\Omega_{\alpha})} \mathbf{p}_{i+1,\Omega_{\alpha}}^k + \mathbf{b}_{\Omega_{\alpha}} + e \dot{\mathbf{g}}_{i,\Omega_{\alpha}})) \quad (20)$$

The algorithm of the entire method is presented here below.

- (i) For the  $i$ -th time step iteration  
 Newton-Raphson iteration step :  $k = 1$   
 Impulse vector :  $\mathbf{p}_{i+1}^k = \mathbf{0}$   
 $\dot{\mathbf{q}}_{i+1}^k = \dot{\mathbf{q}}_i$   
 $\dot{\mathbf{g}}_{i+1}^k = \dot{\mathbf{g}}_i = \mathbf{H}\dot{\mathbf{q}}_i$   
 Eq. (12) DOF contact prediction :  $\hat{\mathbf{g}}_{i+1} = \mathbf{g}_i + \gamma\Delta t \dot{\mathbf{g}}_i$  with  $\gamma = \frac{3}{2}$   
 Identification List of potential contact location :  $\Omega_\alpha = \hat{\mathbf{g}}_{i+1} \leq 0$
- (ii) Kinematic first estimation from *Euler* implicit +  $\theta$  method (with  $\theta = \frac{1}{2}$ )  
 Eq. (7)  $\dot{\mathbf{q}}_{i+\theta}^k = (1 - \theta)\dot{\mathbf{q}}_i + \theta\dot{\mathbf{q}}_{i+1}^k$   
 Eq. (5)  $\mathbf{q}_{i+1}^k = \mathbf{q}_i + \dot{\mathbf{q}}_{i+\theta}^k \Delta t$   
 Eq. (6)  $\mathbf{q}_{i+\theta}^k = (1 - \theta)\mathbf{q}_i + \theta\mathbf{q}_{i+1}^k$
- (iii) Assembling of the tangent operator  $\mathbf{J}^k$ , the internal forces residue with impact  $\hat{\mathbf{R}}^k$  and the impulse residue  $\mathbf{R}_c^k$   
 Eq. (9)  $\mathbf{J}^k = \mathbf{M} + \mathbf{C}_{i+\theta}^{t,k} \theta \Delta t + \mathbf{K}_{i+\theta}^{t,k} \theta^2 \Delta t^2$   
 Eq. (4)  $\mathbf{R}^k = -\mathbf{M}(\dot{\mathbf{q}}^k - \dot{\mathbf{q}}_i) - [\mathbf{C}_{i+\theta}^{t,k} \dot{\mathbf{q}}_{i+\theta}^k + \mathbf{K}_{i+\theta}^{t,k} \mathbf{q}_{i+\theta}^k] \Delta t - \mathbf{G}_i$   
 Eq. (13)  $\hat{\mathbf{R}}_{k+1} = \mathbf{M}(\dot{\mathbf{q}}_{i+1} - \dot{\mathbf{q}}_i) + \mathbf{P}_{i+\theta} \Delta t - \mathbf{G}_i - \mathbf{H}^T \mathbf{p}_{i+1}$   
 $\mathbf{R}_c^k = 1$  to force the entry in the Solving Algorithm
- (iv) Beginning of a Solving Algorithm to annihilate  $\|\hat{\mathbf{R}}^k\|$  and  $\|\mathbf{R}_c^k\|$   
 While  $\|\hat{\mathbf{R}}^k\| > \epsilon$  and  $\|\mathbf{R}_c^k\| > \epsilon_c$  with  $\epsilon$  and  $\epsilon_c$  scalars arbitrarily less than  $10^{-3}$
- (v) Solving operators  
 $\dot{\mathbf{g}}_{i+1}^k = \mathbf{H}\dot{\mathbf{q}}_{i+1}^k$  the relative contact DOF velocities at iteration  $k$   
 Eq. (18)  $\mathbf{b}^k = \mathbf{H}(\mathbf{J}^k)^{-1} \mathbf{R}^k + \dot{\mathbf{g}}_{i+1}^k$   
 Eq. (19)  $\mathbf{W}^k = \mathbf{H}(\mathbf{J}^k)^{-1} \mathbf{H}^T$
- (vi) Calculation of impulse vector  $\mathbf{p}_{i+1}^k$ , (Eqs.(16,17))  
 For  $\alpha \in \Omega_\alpha$   
 $\dot{\mathbf{g}}_\alpha = -e\mathbf{H}\dot{\mathbf{q}}_{i,\alpha}$   

$$\mathbf{p}_{i+1,\alpha}^k = \max \left[ 0, \frac{1}{\mathbf{w}_{\alpha,\alpha}^k} \left( -\mathbf{b}_\alpha^k + \dot{\mathbf{g}}_\alpha - \sum_{\beta \neq \alpha} \mathbf{W}_{\alpha\beta}^k \mathbf{p}_{i+1,\beta}^k + \mathbf{W}_{\alpha\alpha}^k \mathbf{p}_{i+1,\alpha}^k \right) \right]$$
  
 End For Loop
- (vii) New velocity  $\dot{\mathbf{q}}^k$  determination  
 Eq. (13)  $\hat{\mathbf{R}}^k = \mathbf{R}^k + \mathbf{H}^T \mathbf{p}_{i+1}^k$   
 Eq. (8)  $\dot{\mathbf{q}}_{i+1}^{k+1} = \dot{\mathbf{q}}_{i+1}^k - (\mathbf{J}^k)^{-1} \hat{\mathbf{R}}^k$
- (viii) Kinematic update as in (ii), (Eqs. (7,5,6))
- (ix) Update of the tangent operators  $\mathbf{C}_{i+\theta}^{t,k}$ ,  $\mathbf{K}_{i+\theta}^{t,k}$  and  $\mathbf{J}^k$  (Eq. (9)), residue  $\hat{\mathbf{R}}^k$ , (Eq. (4))
- (x) Update of the impulse residue  $\mathbf{R}_c^k$  (Eq.(20))  

$$\mathbf{R}_c^k = \mathbf{p}_{i+1,\Omega_\alpha}^k - \max \left( 0, \mathbf{p}_{i+1,\Omega_\alpha}^k - \rho(\mathbf{W}_{\Omega_\alpha,\Omega_\alpha} \mathbf{p}_{i+1,\Omega_\alpha}^k + \mathbf{b}_{\Omega_\alpha} + e \dot{\mathbf{g}}_{i,\Omega_\alpha}) \right)$$
  
 $k = k + 1$   
 End While Loop  
 $\dot{\mathbf{q}}_i = \dot{\mathbf{q}}_{i+1}^{k+1}$   
 End For Loop

### 3. Bouncing Ball test

The capabilities of the NSCD and PM approaches are compared for a test case of a rigid ball bouncing on a rigid floor (Figure 4). The analytical solution is known from Acary[29], so the parameters used are the same. The ball has a mass  $m = 1\text{kg}$  and is released from a height  $h = 1\text{m}$ , with a zero initial velocity  $V_o = 0$  and vertical acceleration  $g = 2\text{m/s}^2$ .

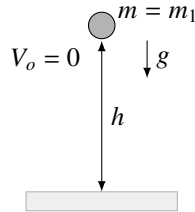


Figure 4: Bouncing ball test case

The LVE and NLVE (Jankowski[14])PM models are tested. A sensitivity analysis is performed to assess the value of the contact stiffnesses  $k_s$  delivering the best results. The mass ratio  $\frac{m_1 m_2}{m_1 + m_2}$  in Table 1 simplified to  $m = m_1$ . Two time steps are chosen,  $10^{-3}\text{s}$  and  $10^{-4}\text{s}$ , to highlight the dependency of the results accuracy on time step, and the study length is fixed to 3.5s. The coefficient of restitution  $e$  equals to 0.5. The figures 5a and 5b present respectively the displacements and velocities of the three approaches, analytical (black curve), NSCD (red dots), and PM (LVE and NLVE in grey curves).

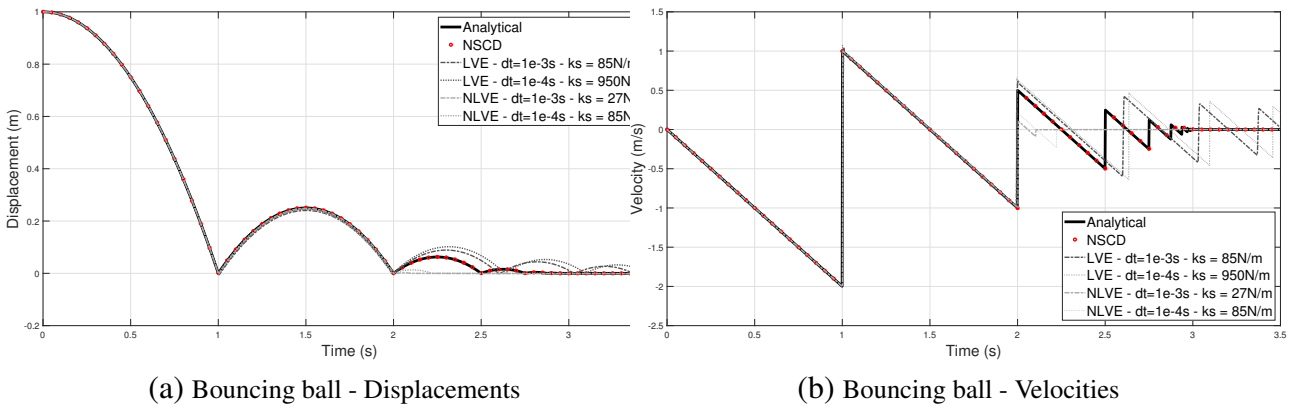


Figure 5: Comparison of the NSCD and PM results for the bouncing ball test case

It is apparent that the NSCD procedure provides the exact response without the need of defining a contact stiffness and no time step to refine. As opposed to the NSCD method, it is highly difficult to reproduce the analytical kinematics with the PM after the second rebound. The out-of-phase motion spotted for  $\Delta t = 10^{-3}\text{s}$  is barely improved by refining it to  $10^{-4}\text{s}$ , and at to the cost of increasing computation time. Also, the impact stiffness yielding the best results changes with time step and the impact law considered. This comparison of both methods is now to be applied in the frame of a scale 1:1 building pounding system.

## 4. Plain Frame Pounding test

### 4.1. Shaking table experimental set-up

In the frame of the ANR SINAPS<sup>1</sup> project to improve knowledge on vulnerability and resistance of strategic buildings (e.g., nuclear power plants) against earthquakes, series of pull back and seismic tries to induce pounding between single-story or two-story structures were carried out at the Commissariat à l’Energie Atomique et aux Energies Alternatives (CEA) de Saclay by Crozet et al.[26, 38, 25].

The two steel-framed structures with rectangular reinforced concrete slabs were fixed side by side to the shaking table AZALEE of the EMSI laboratory<sup>2</sup>. These structures are identified respectively 1 and 2 from left to right (Figure 6b, they can alternatively be set up as one story high (2.5m), or two stories high (5m) by adding or removing additional elements). The gap separation is also adjustable. Finally, to keep the structural motion only in the longitudinal axis, bracing systems (steel cables) are used to limit transverse and torsional displacements (Figures 6a and 6b).

To ensure impact occurrences under seismic motion, the modal responses of both structures are different (Table 6). Thus, one structure is heavier (9200kg versus 7000kg), while the other one is stiffer (HEA140 versus HEA100 steel columns). Sensors are installed on the shaking table, slabs and columns to measure the accelerations with low frequency capacitive accelerometers (0-150Hz) and high-frequency piezoelectric accelerometers (0-4000Hz).

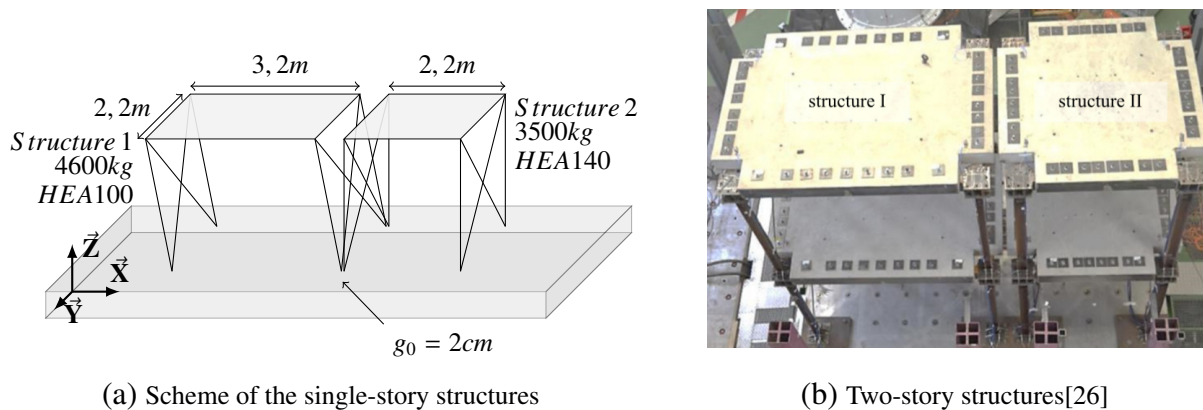


Figure 6: Single-story and Two-story Structures

Four signals were used to excite both single-story and two-story structures, Cadarache (artificial acceleration signal), El Centro (1940), Northridge (1994) and Kobe (1995). Different amplification factors were applied to generate from these signals different Peak Ground Accelerations (PGA) ranging from 0,1g to 0,45g, with g the acceleration of gravity.

### 4.2. Validation of model parameters: Pull back tests

This subsection focuses on determining a value of the coefficient of restitution  $e$  from experimental pull back tests. It also compares results from the NSCD method and PM in a real scale pounding system. Indeed, no consensual formulation has been delivered in the literature to calculate  $e$  before collision, and in most cases its value is defined constant and arbitrary between 0 and 1. Jankowski[39, 16] worked on assessing the variation of the  $e$  with the relative velocities by dropping balls on rigid floors made of different materials. However, Crozet[38], despite confirming the trend of Jankowski curves, pointed out the high difficulty to experimentally assess such value with monitored real

<sup>1</sup>ANR, Agence Nationale de la Recherche, SINAPS, Séisme et Installations Nucléaires, Améliorer et Pérenniser la Sécurité - <https://www.institut-seism.fr/projets/sinaps/>

<sup>2</sup>EMSI Laboratory, Laboratoire d’Etudes de Mécanique Sismique - <http://www-tamaris.cea.fr/index.php>

scale structures. Thus, constant values of  $e$  are assumed in this article.

The pull back tests are done in four steps and only applied to the single-story structures whose slabs are separated by a 2cm average distance  $S$ . First, Structure 1 is fixed to a reference frame by electric suction pads. Secondly, the shaking table is slowly moved longitudinally 2cm to 4cm apart, deforming the columns of Structure 1. The third step is a symmetry check, to verify that the pads each take the same load. Finally, the suction pads power supply is cut off, the left structure is released and is allowed to impact the right-hand side structure. The scheme to illustrate the set-up and data is shown in Figures 6a and 7.

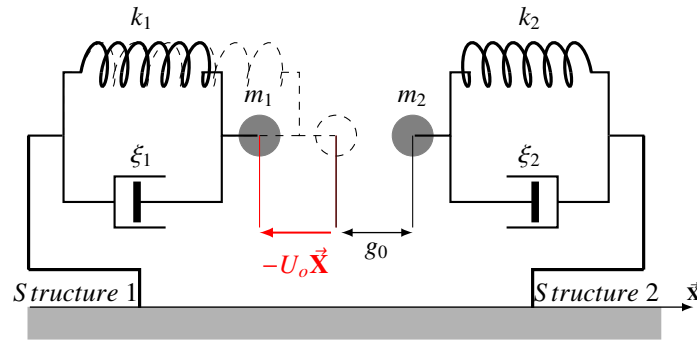


Figure 7: Pull back test SDOF model

In Figure 7,  $m_j$ ,  $\xi_j$  and  $k_j$  are respectively the mass, damping coefficient, and stiffness of the SDOF  $j$ , with  $j = [1;2]$ .  $g_0$  is the separation distance between structures, and  $U_o$  is the pull back distance of the left-hand side structure before its release.

The Linear Visco-Elastic (LVE) model is used herein using Anagnostopoulos[12] approach, as well as the Non-Linear Visco-Elastic models (NLVE) by Jankowski[40] and Khatami[24];  $e$  is fixed at 0.65. Regarding the contact stiffness, it is calibrated in a range centred around the maximum value of  $k_1$  and  $k_2$ . For the NSCD method, results are analysed for values of  $e$  equal to 0.2, 0.6 and 0.9; the time step equals  $10^{-3}$ s. Tables 2 and 3 present the available data and the analytical parameters of the impact models of the structures. Results of the analytical models are then compared with the experimental outcomes.

Table 2: Structural model data

Data	Structure 1	Structure 2
Fundamental Frequency (Hz)	3.50	6.55
Fundamental Period (s)	0.29	0.15
Mass (kg), $m_i$	4600	3500
Longitudinal Stiffness (N/m), $k_i$	2.11e6	5.31e6
Damping Coefficient (%), $\xi_i$	0.4 to 0.6	0.4 to 0.6

Table 3: NSCD and PM parameters

Models	$k_s$ (N/m)	$\xi_d$ (%)	$\xi_r$ (%)	$e$
NSCD method	/	/	/	[0.2;0.6;0.9]
Anagnostopoulos[12]**		8.46e4	0.136	
Jankowski[13, 14]***	[0.01;0.1;1;10;100]max( $k_1, k_2$ )	*	0.373	0.65
Khatami <i>et al.</i> [24]****		*	0.0428	

In Table 3, the contact stiffness  $k_s$  is the multiplication of the coefficient of impact (here taken in [0.01,0.1,1,10,100])

by  $\max(k_1, k_2)$ .

\* The formulation  $\xi_d = 2\xi_r \sqrt{k_s \sqrt{\delta} \frac{m_1 m_2}{m_1 + m_2}}$  with  $\delta$  the interpenetration distance.

\*\* With  $\xi_r$  and  $\xi_d$  expressed in (LVE) in Table 1.

\*\*\* With  $\xi_r$  and  $\xi_d$  expressed as in (NLVE) in Table 1.

\*\*\*\* With  $\xi_r = \frac{(1-e)e^{0.204}}{e^{\alpha+0.204}+3.351e\pi}$  and  $\alpha = 1.05e^{0.653}$ .

Since the transverse and torsional eigenfrequencies of the single-story structures were not available, the finite elements models used for the pull back and seismic tests are respectively SDOF and planar-frame models. They fit the experimental modal and damping behaviour, as observed graphically in Figure 8 and more thoroughly explained in section 4.3.

**NSCD results:** Sixteen pull back tests were performed[38], with pulling distances ranged from 2.1cm to 3.4cm, and six of them were modelled numerically. Different  $e$  values of 0.2, 0.6 and 0.9 were investigated. Figure 8(a) shows, for a pull back test of 2.4cm, the displacements of the two contact degrees of freedom compared with the experimental ones for an  $e$  value of 0.6.

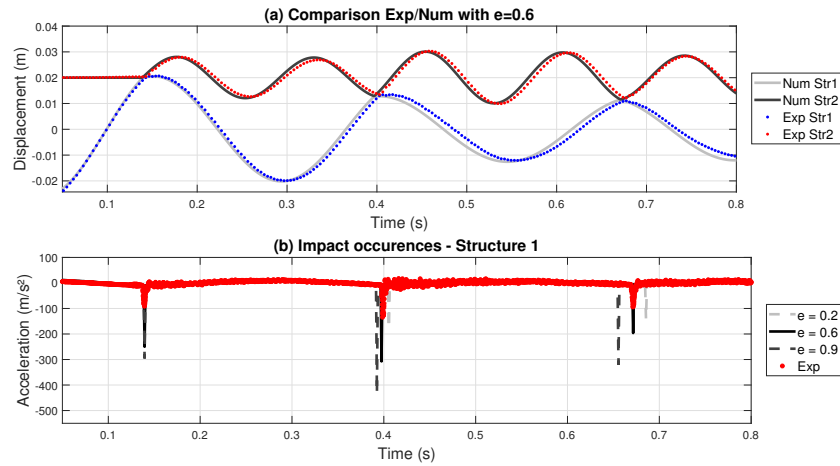


Figure 8: NSCD method : evaluation of  $e$

Matching of the curves is excellent, showing both an accurate impact occurrence, kinematic and damping evolution. These modal and damping parametrizations are then validated and kept for the single-story seismic tests presented in the next section. The Figure 8(b) presents the acceleration of the degree of freedom of the contact node of Structure 2 for values of  $e= 0.2$ , and 0.6 and 0.9. It appears that the value 0.6 is the one giving the exact impact occurrence among the three propositions. The value 0.2 delivering a lower post-impact velocity, the next contact comes later than 0.6. On the other hand,  $e = 0.9$  impacts land quicker than for 0.6 and 0.2. Figure 9 presents the spectra of pseudo-displacements, pseudo-velocities and pseudo-accelerations for Structure 1 (left column) and 2 (right column), and different values of  $e$ . They are compared to the experimental averaged pseudo-accelerations.

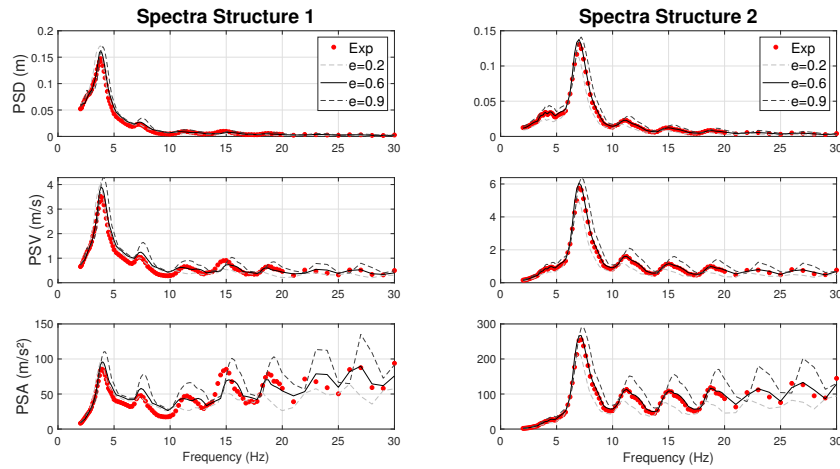


Figure 9: Displacement, velocity and acceleration Spectra for different values of  $e$

The differences are relatively small for the spectra of pseudo-displacements and pseudo-velocities, even with really different values of  $e$ ; the relative error is always lower than 10%. However, differences are significant in the high frequencies of the pseudo-accelerations spectra where both curves of  $e=0.2$  and  $e=0.9$  depart from the experimental curve.

**PM results:** To keep the plots understandable, only the Structure 1 responses are presented in the Figure 10. For  $\Delta t = 10^{-3}s$ , the contact stiffness equal to  $0.01max(k_1, k_2)$  yields the best results for each model, but out-of-phase motion increases at each impact. The amplitudes and impact occurrences are afterwards less and less accurate. Taking a higher stiffness (10 times the highest value of contact stiffness, by Anagnostopoulos[12]), would decrease the phase shift. Nevertheless, it also brings non-realistic kinematic values, unless one takes a much smaller time step and thus increasing the computation cost.

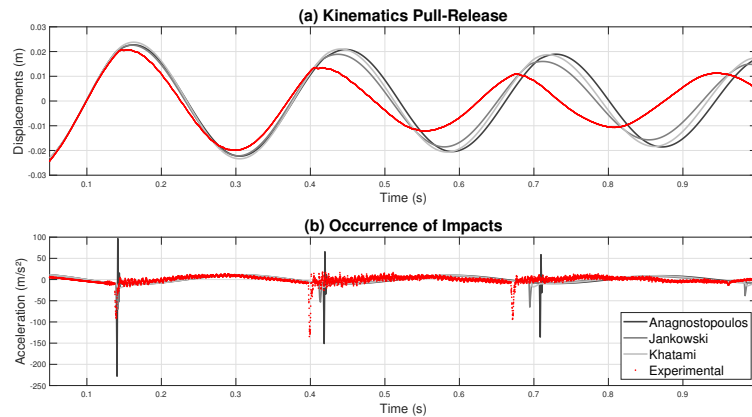


Figure 10: Comparison of PM with experimental values :  $k_s = 0.01max(k_1, k_2)$ ,  $\Delta t = 10^{-3}s$

Figure 11 presents the displacements with a  $10^{-6}$ s time step for Jankowski and Khatami models. Like for the bouncing ball, the contact stiffness yielding the best results vary with the time step and PM used. The new results in dark grey show a better match with the experimental curves, but the computation time is multiplied by a thousand, and major differences remain. Since the kinematics is not good, the spectra studied has been omitted.

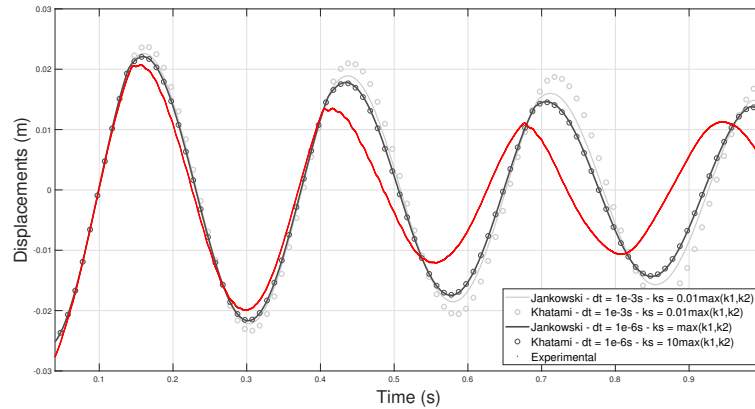


Figure 11: Structure 1 : Effects of  $\Delta t$  and  $k_s$  on results accuracy

Overall in the NSCD method, the value  $e=0.6$  is from now on taken for future calculations. On this particular study case, the NSCD method has proven its accuracy and ergonomics capabilities into yielding outcomes and comparing them to experimental data. Good matching is also possible with PM, but the parameter assessment requires more time. Only the NSCD method will now be tested with seismic tests on single-story frames.

### 4.3. Seismic response of the single-story frames

Figure 12a presents the plane frame finite element model and the structures parameters are the same as for the previous section. The time step calculation equals 0.001s. With a 2cm separation gap, collision is detected for seven signals (Cadarache 0.25g and 0.30g, El Centro 0.4g and 0.45g, Northridge 0.3g and 0.35g, and Kobe 0.4g). Table 4 presents for each case the damping coefficients  $\xi_1$  and  $\xi_2$  of both structures, and the number of impacts simulated numerically and detected experimentally. Damping coefficients  $\xi_1$  and  $\xi_2$  between [0.4;0.6]% computed inside a Superposition Damping matrix[41] yield the best comparison with the experimental results and  $e$  still equals to 0.6.

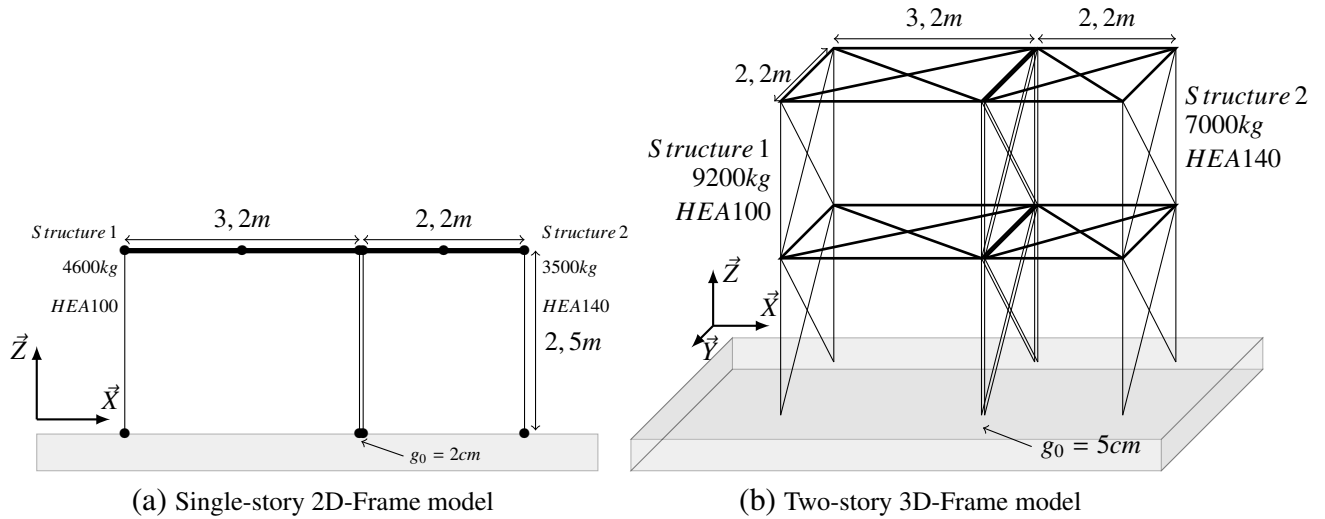


Figure 12: Numerical models used for seismic tests

Table 4: Single-story Structures : Modal damping coefficients and impact occurrences

Signal	$\xi_1 - \xi_2$ (%)	Number of impacts: Numerical/Experimental
Cadarache 0.25g	0.6 - 0.5	9 / 12
Cadarache 0.30g	0.6 - 0.5	8 / 14
El Centro 0.40g	0.5 - 0.5	1 / 3
El Centro 0.45g	0.5 - 0.5	4 / 5
Northridge 0.30g	0.4 - 0.4	2 / 4
Northridge 0.35g	0.4 - 0.4	3 / 3
Kobe 0.4g	0.6 - 0.5	2 / 2

The Cadarache 0.25g test is now analysed. It yields very interesting results, especially considering the important number of impacts for the Cadarache signals. Indeed, in this case, the number of impact is high (12) and the simulation delivered 9 of them, always at right times, which shows the good treatment of the impact of the algorithm. As a matter of fact, even after several collisions and potential sources of divergences, the model outcomes kept matching the real displacements. The figure displays the numerical and experimental comparison in displacements (upper figure) and accelerations peaks due to collisions (lower figure). The six remaining signal comparisons are presented in Appendix 5.

Nine of the first ten impacts happen at the exact right instant, and the only one missing (close to 9s) has a small amplitude compared to the others. Since the accelerations peak from the sensors is small, barely noticeable, it can suggest that the structures simply brushed past each other, barely triggering the sensors. Structure 1 numerical displacements are smaller in amplitude starting at 16s, leading to the two remaining contacts not detected (18s and 22s).

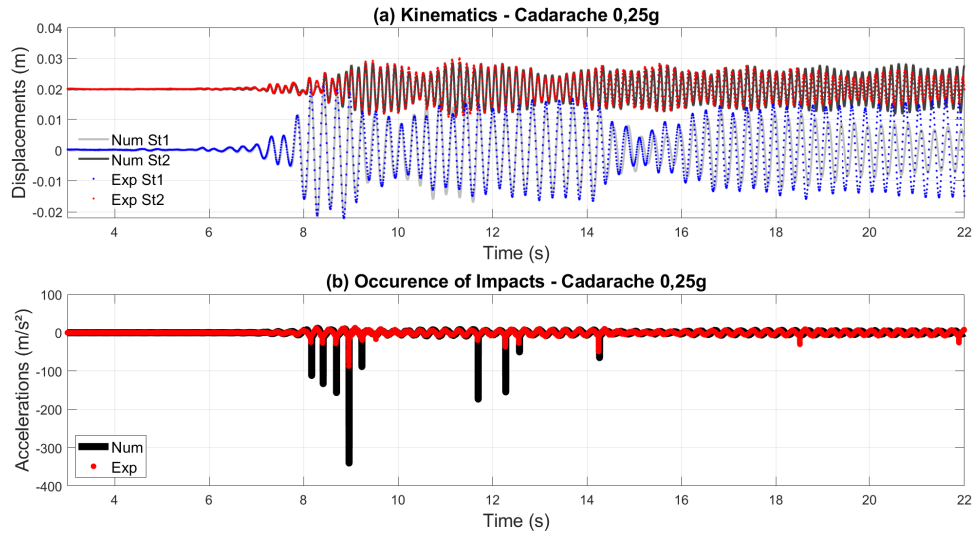
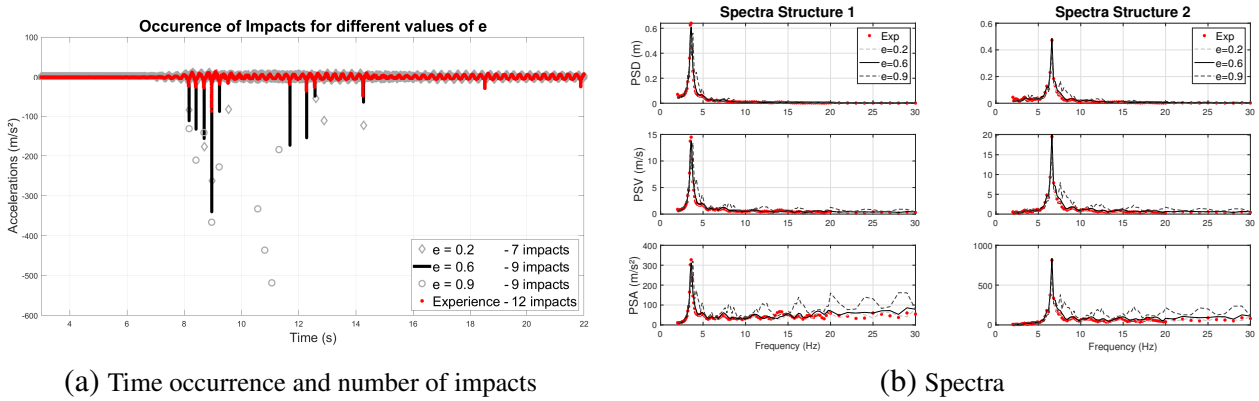


Figure 13: Single-story results (Cadache 0.25g signal) : numerical versus experimental comparison

A parametric analysis of  $e$  on this same Cadache 0.25g test is presented on Figures 14a and 14b. They compare both numerically and experimentally the time occurrence and the number of impacts along with the spectra of the two structures, respectively.



(a) Time occurrence and number of impacts

(b) Spectra

Figure 14: Sensitivity analysis of  $e$  : Cadache 0.25g on single-story structures

First in Figure 14a, there is a noticeable change in the number and time instants of the impacts with the coefficient of restitution. Among the twelve collisions expected (red dots), only seven and nine are respectively reproduced for the  $e$  values of 0.2 and 0.9 (grey markers). Even more for  $e=0.9$ , four impacts occur where there is no impact evidence between 10s and 12s. The value of 0.6 yields once again the better match. Regarding the spectra of Figure 14b, the peak values of pseudo-displacements, pseudo-velocities, pseudo-accelerations and the general trend of the curves are quite accurate, especially around the fundamental frequencies. Discrepancies appear after 10Hz, but only with the  $e$  value of 0.9.

Overall, taking a constant value of 0.6 for  $e$  yields once again good results, both in terms of kinematics and spectral trends for all the seven different signal comparisons (c.f plots in Appendix 5).

#### 4.4. Seismic response of the two-story frames

For the two-story structures separated by a 5cm distance, pounding occurred for the following signals: Cadarache 0.45g, El Centro 0.3g, Northridge 0.2g, and Kobe 0.2g and 0.25g. Because the experimental transverse and torsional eigenfrequencies were available, a 3D-fiber model is used to better model the structures. Figures 6b and 12b show the real scale and numerical models of the frames respectively. Each structure is composed of fourteen nodes and thirty two elements. The NSCD method is applied in between the two close corners of each slab so that eight degrees of freedom are involved into the contact detection. The time step calculation is kept at  $10^{-3}$ s. Furthermore, average experimental displacements are obtained from the double integration of the four acceleration piezoelectric sensors on the slab.

**Sources of discrepancy:** one source of discrepancy comes from the correct evaluation of the damping and modal behaviour. During the experiments, three different tests were carried out to determine the real eigenfrequencies and damping coefficients of each fundamental mode of the structures. They are denoted from the Covariance Driven Stochastic Sub-Space Identification (SSI-COV) white noise analysis, a second one with a decremental logarithmic analysis (SSI-COV (DLA)), and a hammer test. According to Crozet *et al.*[38], the SSI-COV (DLA) values applied to their own model yielded the best comparisons. Unfortunately, in our case the damping coefficients of the second transverse and torsional modes could not be obtained. As a first approximation, they are taken here equal to the first transverse and torsional coefficient respectively. A damping superposition matrix[41] is computed on each structure so that their dynamic behaviour is as similar as possible with the experimental one. Table 5 presents the values of damping coefficients finally identified, and Table 6 presents the matching of the numerical eigenfrequencies with the experimental ones. **L. B.**, **Tr. B.**, and **To.** signify respectively the Longitudinal Bending, Transverse Bending, and Torsion modes.

Table 5: Experimental Damping Coefficients  $\xi$  from SSI-COV (DLA) test[26, 38]

	1 <sup>st</sup> L. B.	2 <sup>nd</sup> L. B.	1 <sup>st</sup> Tr. B.	2 <sup>nd</sup> Tr. B.	1 <sup>st</sup> To.	2 <sup>nd</sup> To.
$\xi$ (%) Structure 1	0.7	0.2	1.3	<b>1.3</b>	2.0	<b>2.0</b>
$\xi$ (%) Structure 2	1.0	0.2	1.0	<b>1.0</b>	3.0	<b>3.0</b>

Table 6: Experimental and Numerical eigenfrequencies

	1 <sup>st</sup> L. B.	2 <sup>nd</sup> L. B.	1 <sup>st</sup> Tr. B.	2 <sup>nd</sup> Tr. B.	1 <sup>st</sup> To.	2 <sup>nd</sup> To.
Structure 1 Exp (Hz)	2.10	5.60	6.10	17.5	8.60	24.4
Structure 1 Model (Hz)	2.10	5.60	6.11	17.5	8.60	24.4
Structure 2 Exp (Hz)	3.70	10.4	8.20	25.2	10.1	28.0
Structure 2 Model (Hz)	3.69	10.4	8.20	25.2	10.2	28.0

Also, set-up imperfections may create an unplanned motion of the frames. As spotted during the experimental campaign[26, 38], the planar surfaces where pounding occurs are not perfectly aligned. The gap separations of the two ends are different, one being 5cm and the other 5.5cm. This one important parameter corrupt the experimental kinematic response, creating non-planar and torsional motion. To reproduce the torsional peaks of the experimental pseudo-spectra plots, different separation gaps in the range between 4.0cm and 6.0cm were chosen, with a maximum of  $\pm 0.5$ cm difference between the two contact corners gaps.

For the five tests involving pounding, Table 7 displays the asymmetric gap and the number of impacts simulated numerically and detected experimentally. The gaps displayed are the ones, inside the range [4.0;6.0]cm, yielding the best comparison with the experimental results.

Table 7: Impact occurrences

Signal	Gaps of Left/Right corners (cm)	Number of impacts: Numerical/Experimental
Cadarache 0.45g	5 / 5.5	3 / 3
El Centro 0.30g	5 / 5.5	3 / 3
Northridge 0.20g	5.5 / 6	1 / 1
Kobe 0.20g	4.5 / 5	3 / 3
Kobe 0.25g	5 / 5.5	3 / 4

The Kobe 0.25g second floor results are presented here below. The four remaining signals responses, Cadarache 0.45g, El Centro 0.30g, Northridge 0.20g and Kobe 0.20g, are included in Appendix 5. Due to the 3D nature of the models, it is possible to plot the displacements of the four facing corners, two of them called "left corners", and two others "right corners". For a sake of readability, only the displacements and accelerations of the left corner are plotted in Figure 15.

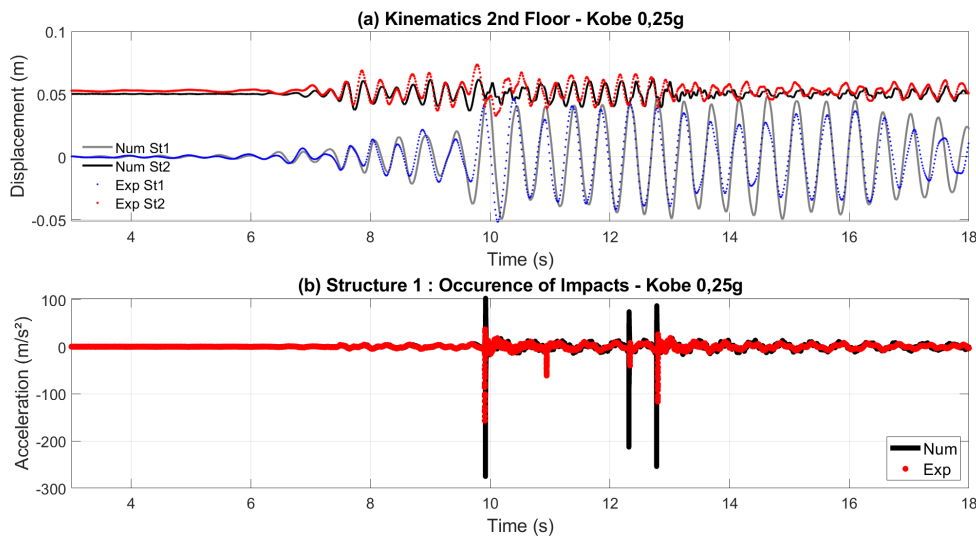


Figure 15: Two-story results (Kobe 0.25g signal) : numerical versus experimental comparison

Figure 15 shows good agreement of kinematic responses and impact occurrences between experimental and numerical outcomes. One impact was not reproduced at 11s, and by checking the displacements, it was missed by a few millimeters.

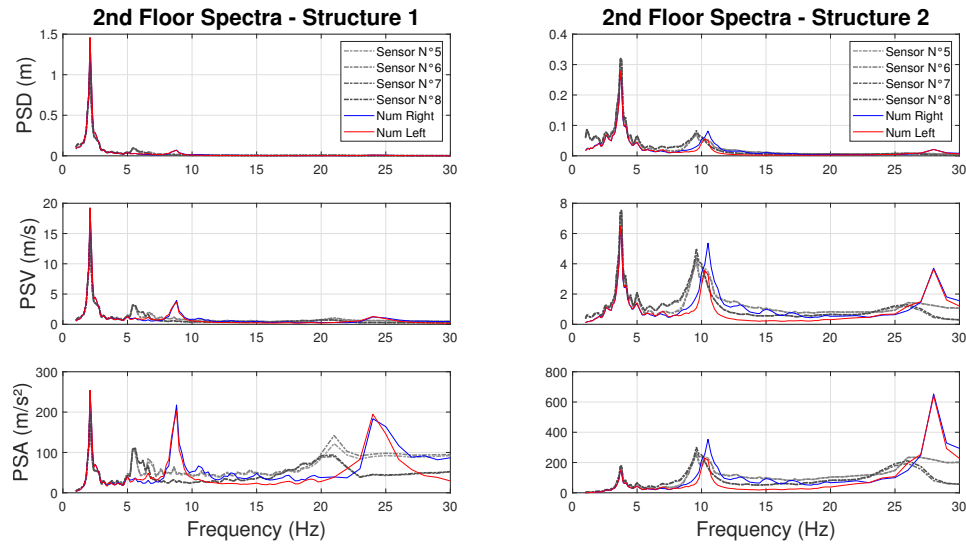


Figure 16: Two-story (Kobe 0.25g signal) Spectra : numerical versus experimental comparison

Figure 16 compares the numerical versus experimental spectra. Herein, the data extracted from the sensors are not averaged so that torsional effects are visible. Overall, the general trend of the pseudo-displacements and pseudo-velocities are well reproduced for all signals, especially around the fundamental frequency. Bigger differences appear in the high frequencies, more notably from the pseudo-accelerations presented in Figure 16. The triggering of the first and second torsional mode are now observable both numerically because structures were misaligned as for the experimental configurations. First, the experimental second torsional frequency is lower than the one numerically targeted during the modal configuration. Indeed, for Structure 1, the peak is triggered around 22Hz while it was estimated at 24,4Hz by the SSI-COV (DLA) tests (26Hz rather than 28Hz for Structure 2). The same happened with the four remaining signals (see Appendix 5). The inferred modal eigenfrequencies were probably slightly different than the real ones. Finally, the peak amplitudes in high frequencies are very different. It can be explained by the uncertainties on the slab alignment, which has an important effect on the amplitude of the torsional mode peak.

## 5. Discussion

This article presents a numerically efficient algorithm for solving the equations of motion of structural systems subjected to pounding, herein referred to the NSCD method. The algorithm is an implicit Moreau-Jean integration scheme combined with Newton's law of impacts, which relies on the coefficient of restitution  $e$  and accounts for energy dissipation upon contact. To illustrate the accuracy and robustness of the NSCD approach, two application examples are presented: (i) a bouncing ball test, and a (ii) building collision test, where NSCD-based solutions are compared with shaking table test results. From this study, the following conclusions can be drawn:

- The NSCD solution to the bouncing ball problem yields the exact analytical solutions, even with larger time steps. On the other, the Penalty Method (PM) yields similar results at the expense of shorter time step and larger computational effort.
- The NSCD method matched reasonably well the experimental results of 2 two-story buildings in terms of amplitude and phase of the displacement histories, as well as pounding occurrences. The response spectra (e.g., PSD, PSV, PSA) around the fundamental frequency of each buildings is captured accurately by the numerical scheme; however, some differences are apparent in higher frequencies. Among several factors, these differences can be attributed to small accidental slab misalignments observed in the experiments, and the inferred modal damping values. These numerical simulations relied on a constant  $e$  value, which is also a source of uncertainties.
- A sensitivity analysis was performed and an  $e$  value of 0.6 resulted in very good agreement between the numerical and experimental response. With high quality experimental data and under the assumption of a constant value for  $e$ , this calibration process is straightforward as the number of empirical parameters is reduced to a minimum. In contrast, finding the correct stiffness coefficient, damping ratio, and integration time step on a PM implementation is cumbersome.

Overall, the NSCD method is a very useful tool for building pounding analyses and a good complement to traditional penalty method approaches. Work is underway to evaluate the effect of pounding in the context of performance-based design and risk analysis.

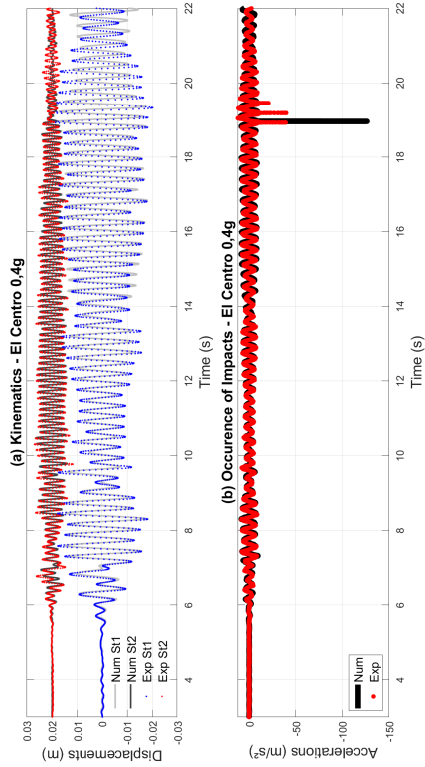
## Acknowledgments

This work is partly funded by an CDSN Grant (Contrat Doctoral Spécifiques aux Normaliens) and the ECOS-Sud Grant for international collaboration CONICYT-ECOS170044.

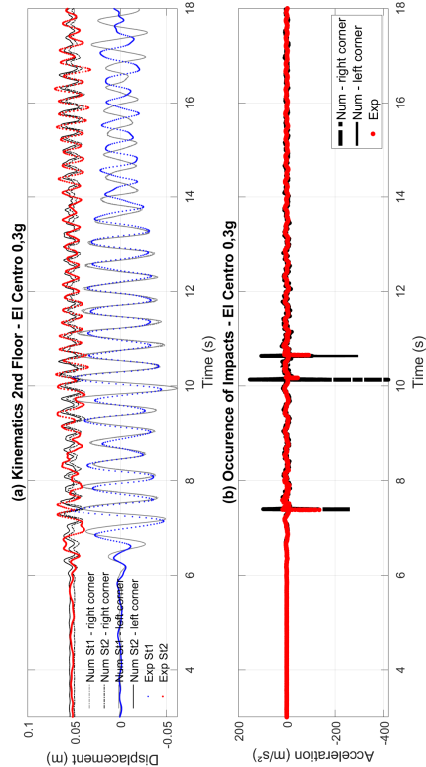
The authors deeply thanks V. Crozet of the French CEA for the provisioning of the experimental data[38]. Many thanks are also addressed to V. Acary and F. Bourrier of the IRSTEA<sup>3</sup> for their guidance into the NSCD method use. Dr. Candia received support from Facultad de Ingeniería Civil at Universidad del Desarrollo - Chile, FONDECYT Grant 11180937 "Seismic Risk of Mined Tunnels", the National Research Center for Integrated Natural Disaster Management FONDAP/CIGIDEN 15110017, and FONDECYT Grant Number 1170836, "SIBER-RISK: Simulation Based Earthquake Risk and Resilience of Interdependent Systems and Networks." The authors are grateful for this support.

---

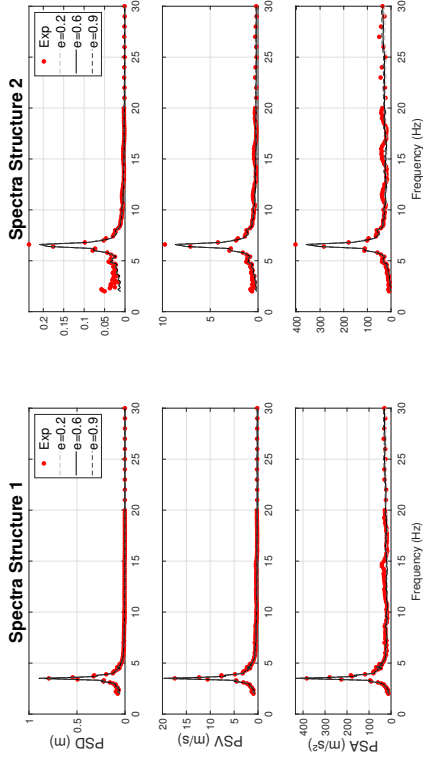
<sup>3</sup>IRSTEA, Institut national de Recherche en Sciences et Technologies pour l'Environnement et l'Agriculture.



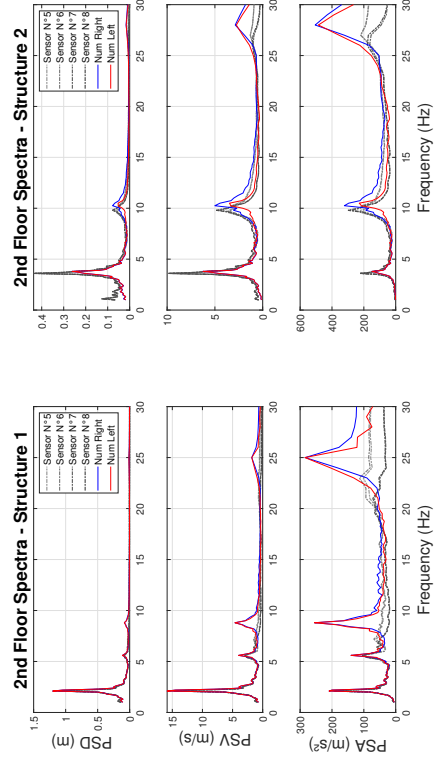
(a) Single-story : El Centro 0.40g num/exp comparison - e = 0.6



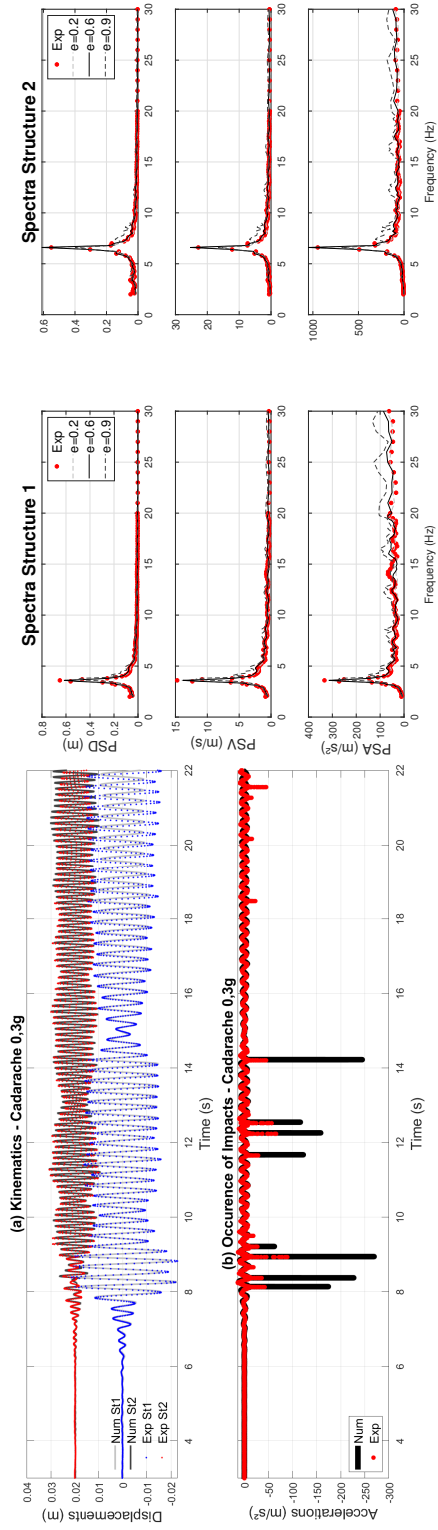
(c) two-story : El Centro 0.30g num/exp comparison



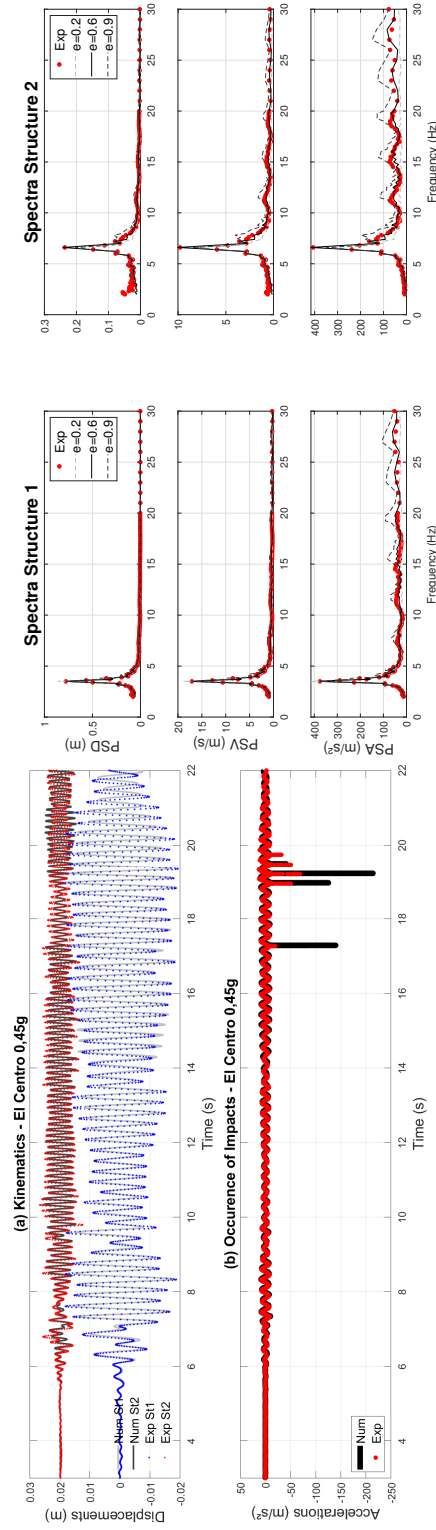
(b) Single-story : Spectra El Centro 0.40g num/exp comparison



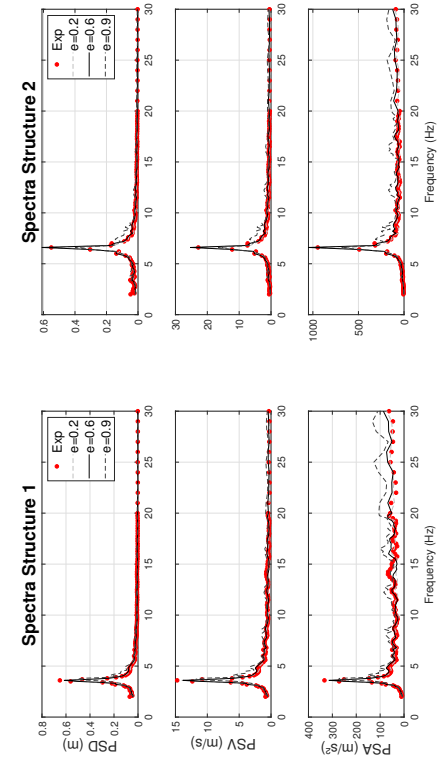
(d) two-story : Spectra El Centro 0.30g num/exp comparison



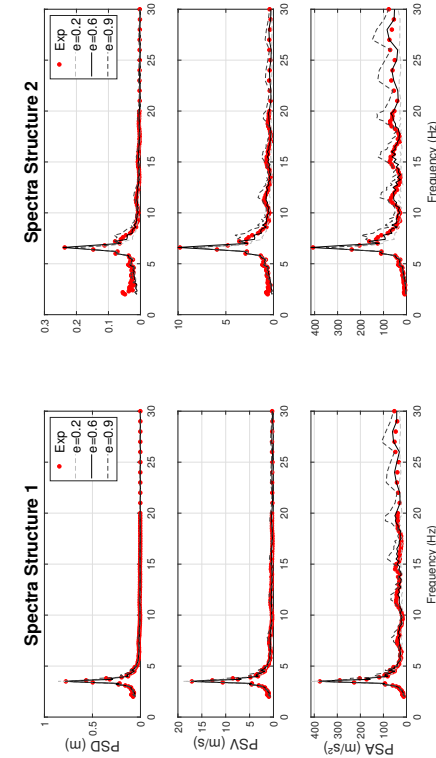
(a) Single-story structures - Cadarache 0.3g - Kinematics



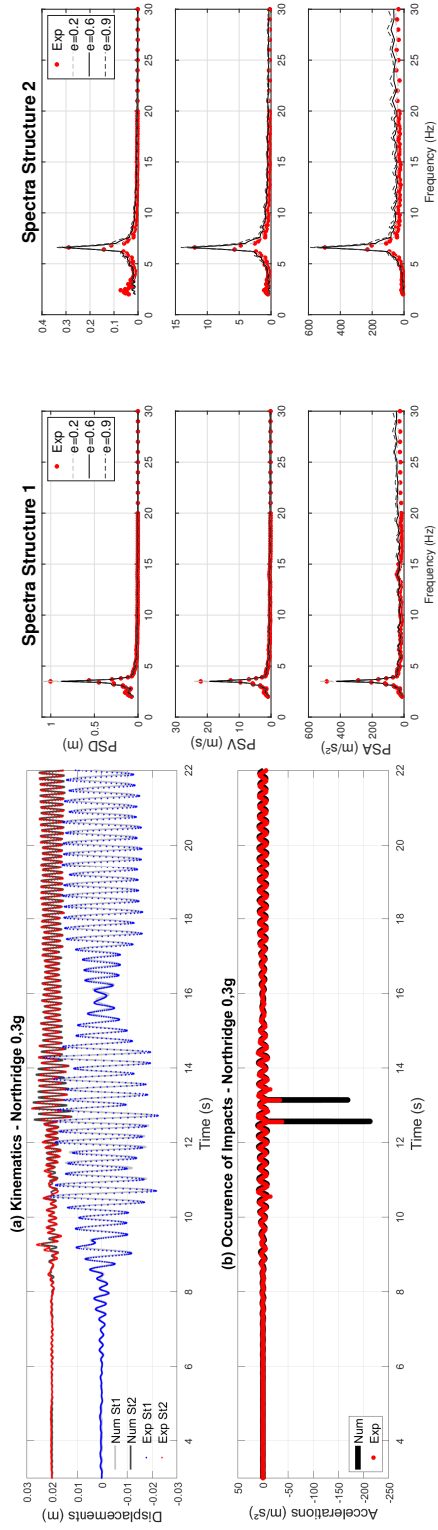
(c) Single-story structures - El Centro 0.45g - Kinematics



(b) Single-story structures - Cadarache 0.3g - Spectra

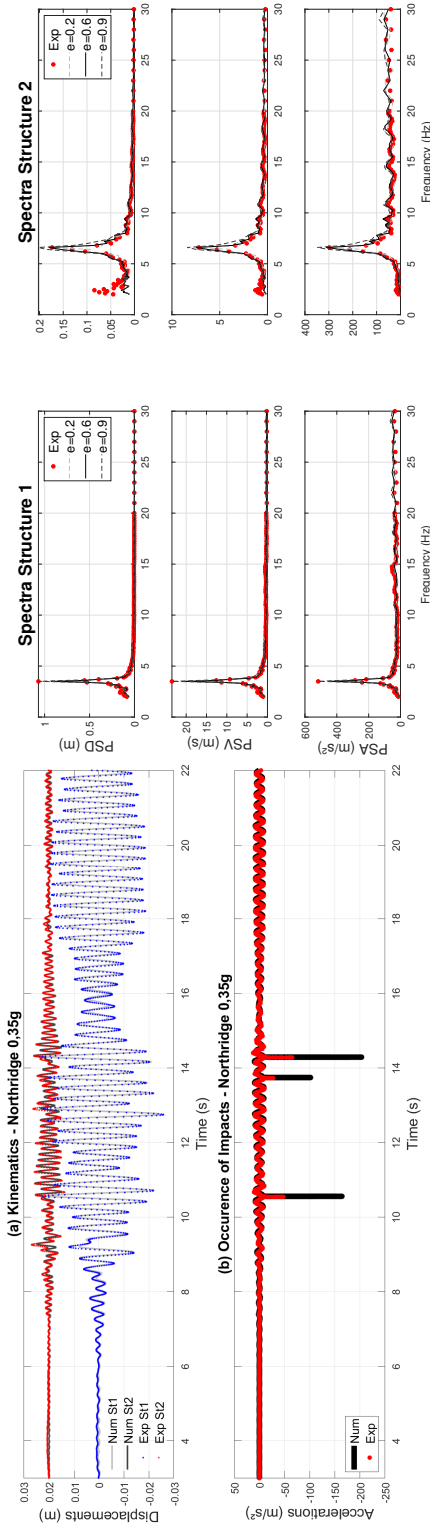


(d) Single-story structures - El Centro 0.45g - Spectra



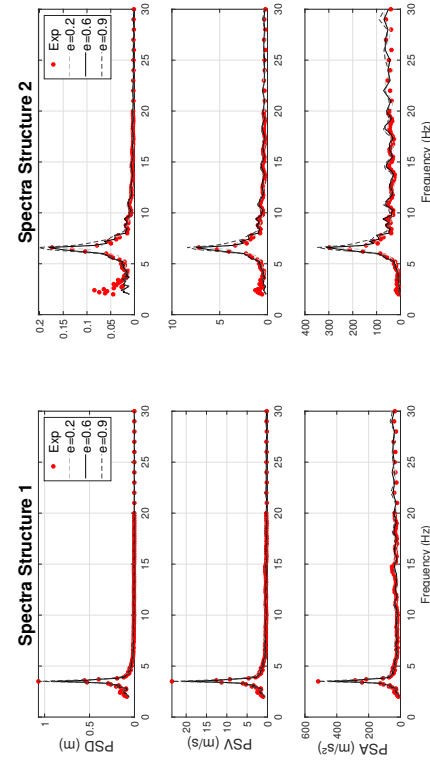
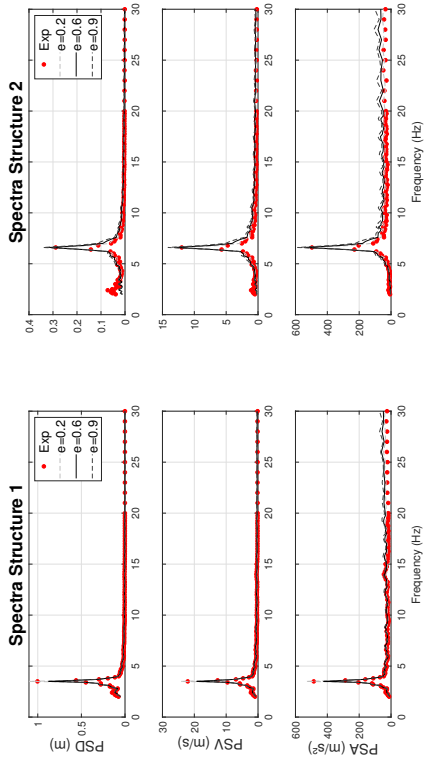
(a) Single-story structures - Northridge 0.3g - Kinematics

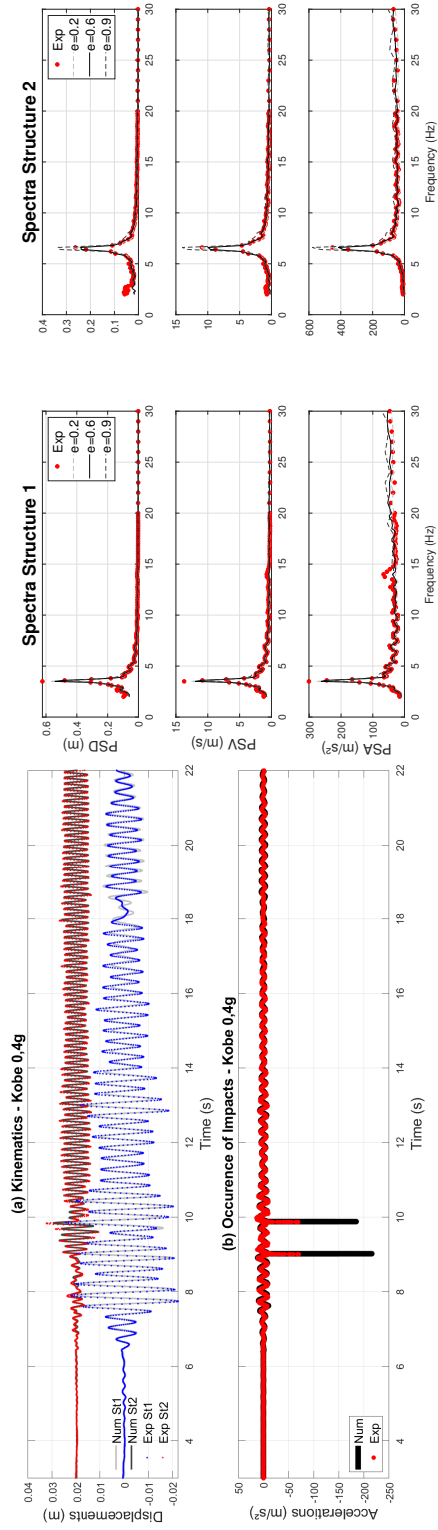
(b) Single-story structures - Northridge 0.3g - Spectra



(c) Single-story structures - Northridge 0.35g - Kinematics

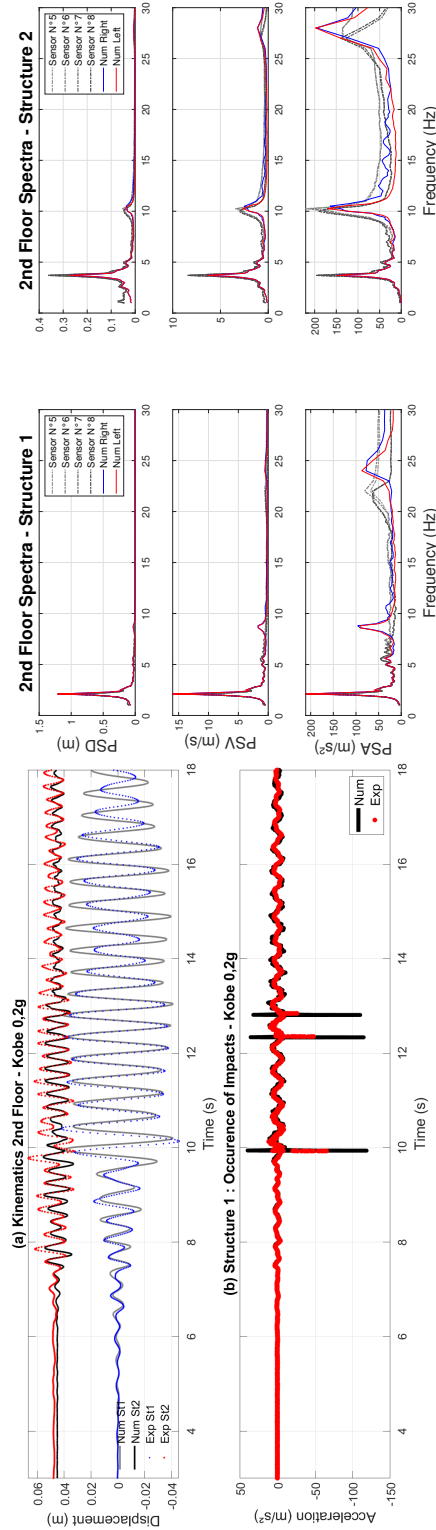
(d) Single-story structures - Northridge 0.35g - Spectra





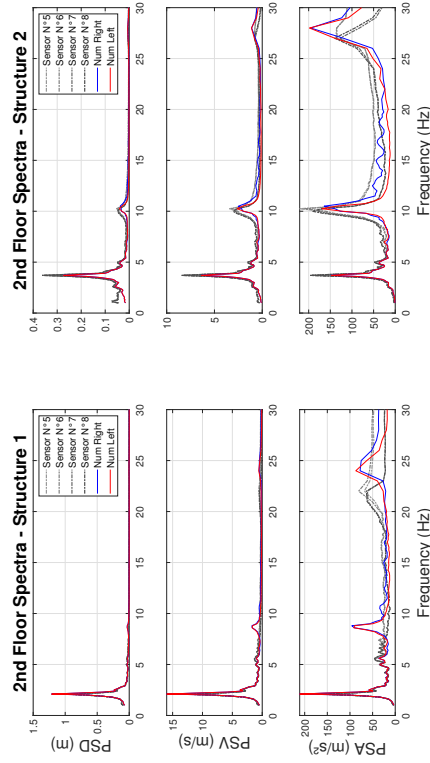
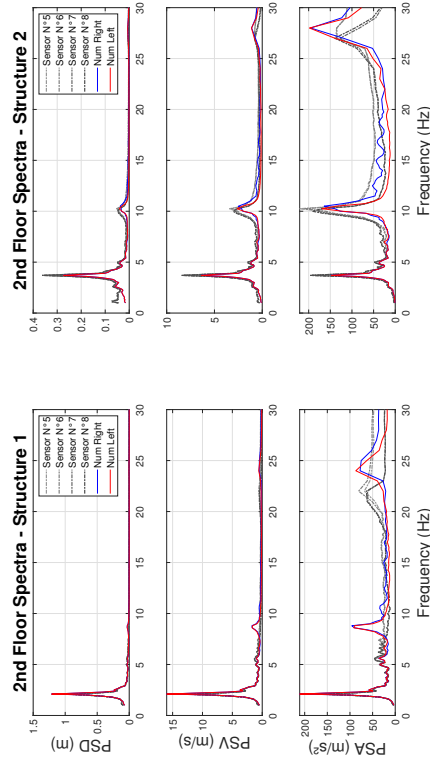
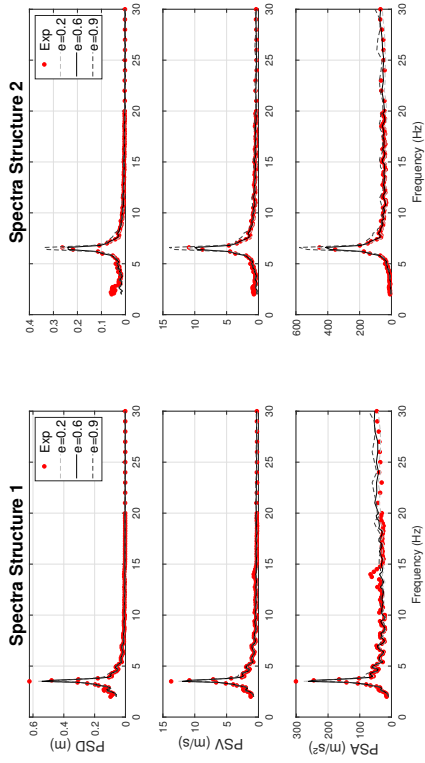
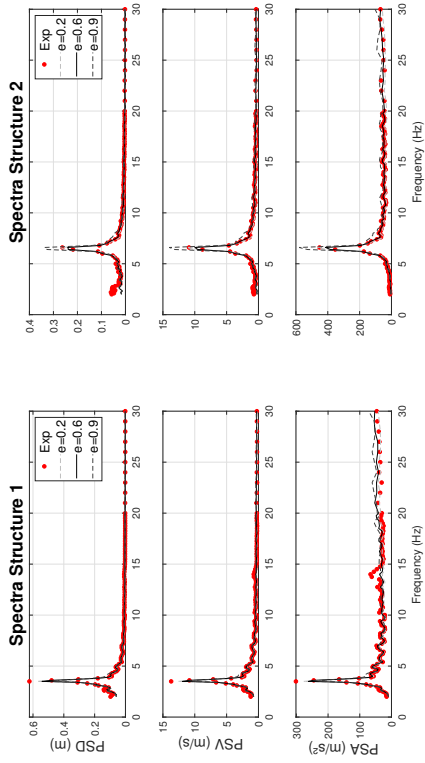
(a) Single-story structures - Kobe 0.4g - Kinematics

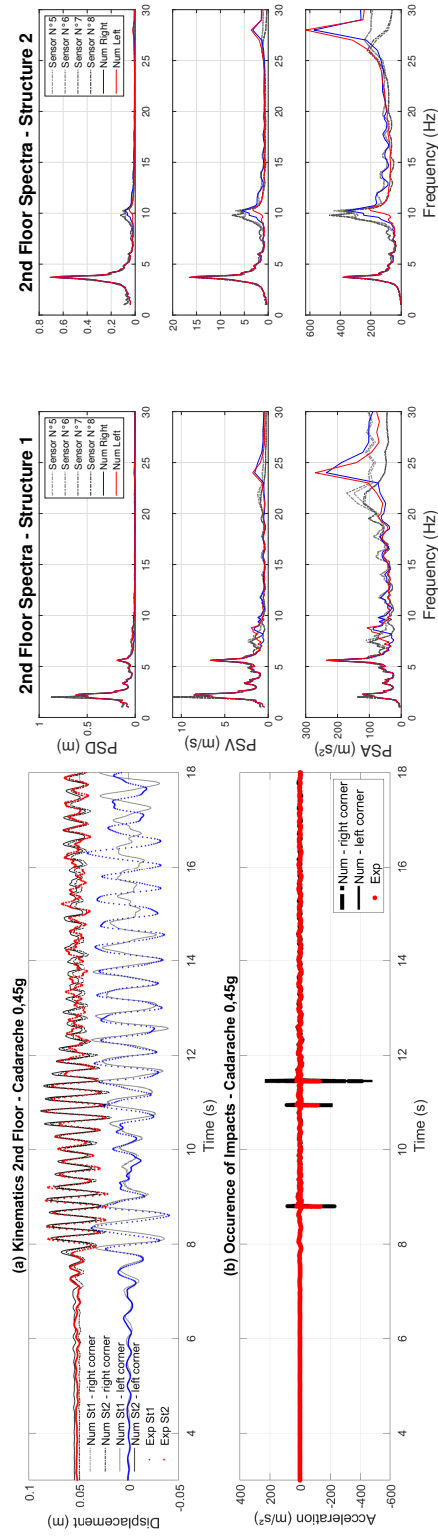
(b) Single-story structures - Kobe 0.4g - Spectra



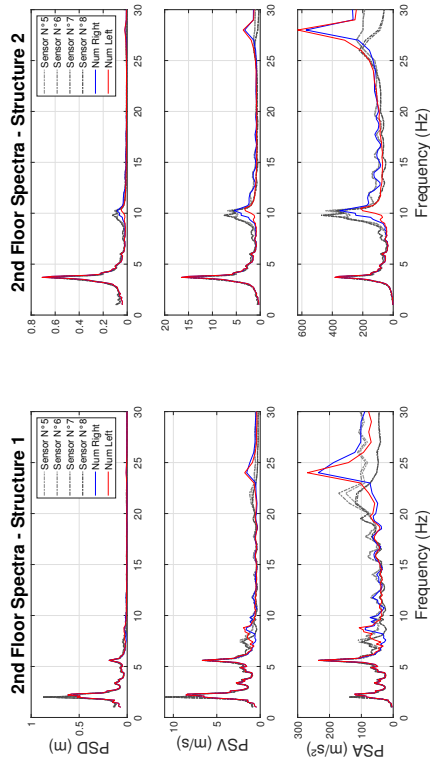
(c) two-story structures - Kobe 0.20g - Kinematics

(d) two-story structures - Kobe 0.20g - Spectra

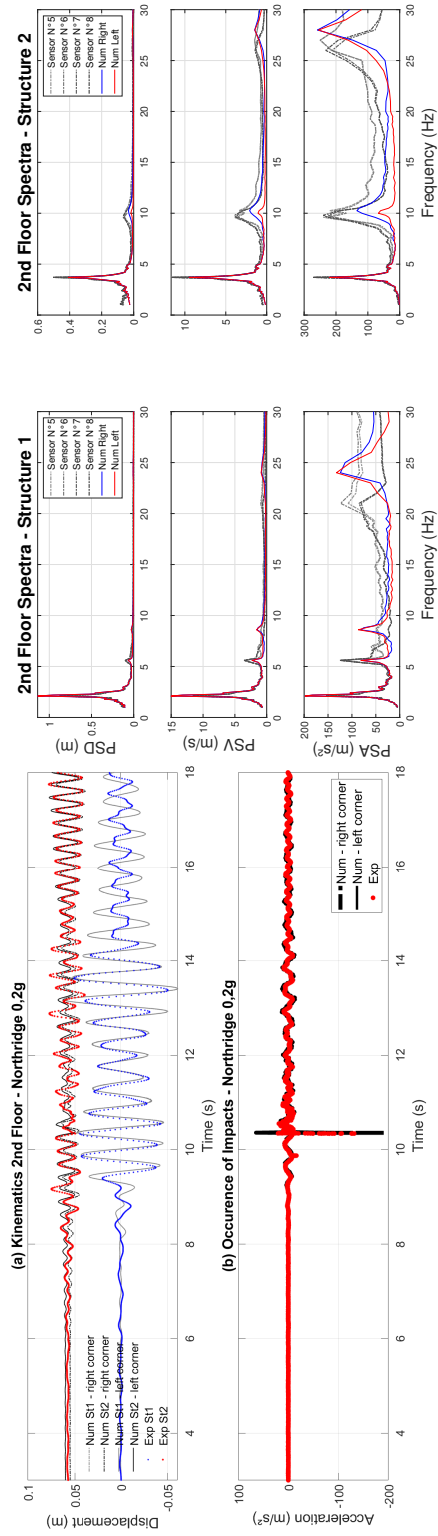




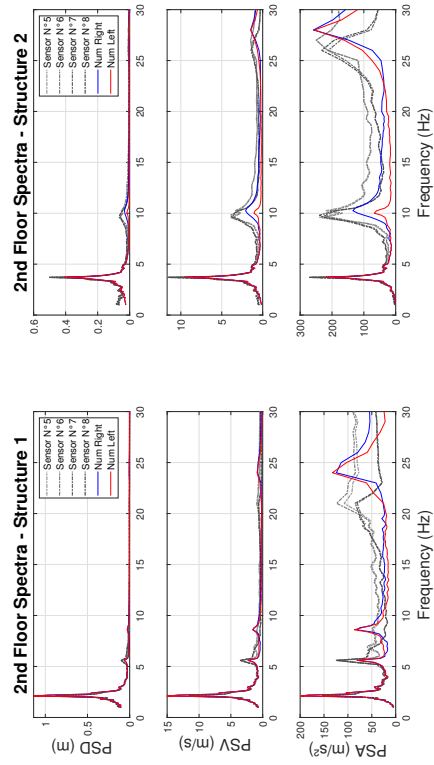
(a) two-story structures - Cadarache 0.45g - Kinematics



(b) two-story structures - Cadarache 0.45g - Spectra



(c) two-story structures - Northridge 0.20g - Kinematics



(d) two-story structures - Northridge 0.20g - Spectra

## References

- [1] A. I. C. on the 1985 Mexico City Earthquake (Ed.), Observations on structural pounding. Proceedings ASCE International Conference on the 1985 Mexico City Earthquake.
- [2] Rosenblueth, Meli, Observations of the performance of buildings during the 1985 Mexico earthquake, and structural design implications, International Journal of Mining and Geological Engineering.
- [3] K. Kasai, B. Maison, Building pounding damage during the 1989 Loma Prieta earthquake, Engineering Structures - Elsevier.
- [4] E. Reinoso, P. Quinde, L. Buendía, P. Ramos, Intensity and damage statistics of the September 19, 2017 Mexico earthquake: influence of soft story and corner asymmetry on the damage reported during the earthquake.
- [5] C. Arnold, Pounding damage at Hotel de Carlo (https://nisee.berkeley.edu/elibrary/image/201307115).
- [6] H. Sezen, Note effect on pounding (https://nisee.berkeley.edu/elibrary/image/izt-484).
- [7] V. Jeng, W. Tzeng, Assessment of seismic pounding hazard for Taipei city, Engineering Structures.
- [8] 11th World Conference on Earthquake Engineering (Ed.), Implications of observed pounding of buildings on seismic code regulations.
- [9] ASCE Standard-ASCE/SEI 7-16: Minimum design loads for buildings and other structures.
- [10] S. Anagnostopoulos, Building pounding re-examined: How serious a problem is it?, Elsevier.
- [11] S. Anagnostopoulos, Equivalent viscous damping for modeling inelastic impacts in earthquake induced pounding problems, Earthquake Engineering and Structural Dynamics.
- [12] S. Anagnostopoulos, Pounding of buildings in series during earthquakes, Earthquake Engineering and Structural Dynamics.
- [13] R. Jankowski, Analytical expression between the impact damping ratio and the coefficient of restitution in the non-linear viscoelastic model of structural pounding, Wiley : Earthquake Engineering and Structural Dynamics.
- [14] R. Jankowski, Comparison of numerical models of impact force for simulation of earthquake-induced structural pounding, Springer.
- [15] M. M. K. Choong, R. Jankowski, Seismic pounding between adjacent buildings: Identification of parameters, soil interaction issues and mitigation measures, Elsevier : Soil Dynamics and Earthquake Engineering.
- [16] R. Jankowski, S. Mahmoud, Earthquake-induced structural pounding, 2015.
- [17] H. Naderpour, R. Barros, R. Jankowski, Numerical study on pounding between two adjacent buildings under earthquake excitation, in: H. P. Corporation (Ed.), Shock Vibration, Volume 16, Hindawi, 2015.
- [18] X. Xu, X. Xu, A new formula of impact stiffness in linear viscoelastic model for pounding simulation, Shock and Vibration.
- [19] M. Papadrakakis, H. Mouzakis, A Lagrange multiplier solution method for pounding of buildings during earthquakes, Earthquake Engineering and Structural Dynamics.
- [20] M. Papadrakakis, C. Apostopoulou, Three-dimensional simulation of structural pounding during earthquakes, Journal of Engineering Mechanics.
- [21] G. Cole, The effects of details analysis on the prediction of seismic building pounding performance (2012).
- [22] J. Kranhenbuhl Ambiel, M. Brun, P. Faye, Entreochoquement de dalles en béton armé pour des structures soumises à un chargement sismique, AFPS 2019 La société face au risque sismique: Connaissance, protection et gestion de crise, Strasbourg, 2019.
- [23] G. Candia, J. C. De La Llera, J. L. Almazan, A physical model for dynamic analysis of wine barrel stacks, Earthquake Engineering & Structural Dynamics.
- [24] S. Khatami, H. Naderpour, R. Barros, A. Jakubczyk-Galczyńska, R. Jankowski, Effective formula for impact damping ratio for simulation of earthquake-induced structural pounding, Geosciences.
- [25] V. Crozet, I. Politopoulos, Sensitivity analysis of pounding between adjacent structures, Wiley.
- [26] V. Crozet, I. Politopoulos, M. Yang, J. Martinez, S. Erlicher, Shake table tests of structures subject to pounding, Wiley : Earthquake Engineering & Structural Dynamics 47 (2018) 219–235.
- [27] S. Khatiwada, N. Chouw, Limitations in simulation of building pounding in earthquakes, International Journal of Protective Structures.
- [28] V. Acary, B. Brogliato, Numerical Methods for Nonsmooth Dynamical Systems, 2008.
- [29] V. Acary, Projected event-capturing time-stepping schemes for nonsmooth mechanical systems with unilateral contact and Coulomb's friction, Computer methods in applied mechanics and engineering.
- [30] J. Moreau, Standard inelastic shocks and the dynamics of unilateral constraints, Springer 288 (1985) 173–221.
- [31] M. Jean, The non-smooth contact dynamics method, Computer methods in applied mechanics and engineering.
- [32] V. Acary, Energy conservation and dissipation properties of time-integration methods for nonsmooth elastodynamics with contact, ZAMM - Journal of Applied Mathematics and Mechanics.
- [33] V. Acary, Contribution à la modélisation mécanique et numérique des édifices maçonnés (2001).
- [34] Hertz, Ueber die Ausbreitungsgeschwindigkeit der elektrodynamischen Wirkungen.
- [35] Goldsmith, The Theory and Physical Behaviour of Colliding Solids.
- [36] K. Ye, L. Li, A modified Kelvin impact model for pounding simulation of base-isolated building with adjacent structures, Earthquake Engineering and Engineering Vibration.
- [37] M. Migda, M. Szczepanski, N. Lasowicz, Non-linear analysis of inter-story pounding between wood-framed buildings during ground motion, Geosciences.
- [38] V. Crozet, Etude de l'entreochoquement entre bâtiments au cours d'un séisme (2019).
- [39] R. Jankowski, Experimental study on earthquake-induced pounding between structural elements made of different building materials, Wiley : Earthquake Engineering and Structural Dynamics.
- [40] R. Jankowski, Pounding force response spectrum under earthquake excitation, Elsevier : Engineering Structures.
- [41] A. Chopra, Dynamics of Structures 4th Edition, 2012.